



1 **Composition and mixing state of atmospheric aerosols determined by**
2 **electron microscopy: method development and application to aged Saharan**
3 **dust deposition in the Caribbean boundary layer**

4 Konrad Kandler¹, Kilian Schneiders¹, Martin Ebert¹, Markus Hartmann^{1,*}, Stephan Weinbruch¹,
5 Maria Prass², Christopher Pöhlker²

6 ¹Institute for Applied Geosciences, Technical University Darmstadt, 64287 Darmstadt, Germany

7 ²Max Planck Institute for Chemistry, Multiphase Chemistry Department, 55128 Mainz, Germany

8 ^{*}now at: Experimental Aerosol and Cloud Microphysics Department, Tropos Leibniz-Institute für
9 Tropospheric Research (TROPOS), 04318 Leipzig, Germany

10

11 *Correspondence to:* K. Kandler (kandler@geo.tu-darmstadt.de)

12

13

14 **Abstract.** The microphysical properties, composition and mixing state of mineral dust, sea-salt and
15 secondary compounds were measured by active and passive aerosol sampling followed by electron
16 microscopy and X-ray fluorescence in the Caribbean marine boundary layer. Measurements were
17 carried out at Ragged Point, Barbados during June/July 2013 and August 2016. Techniques were
18 developed to conclude from collected aerosol on atmospheric concentrations and aerosol mixing-
19 state, and different models were compared. It became obvious that in the diameter range with the
20 highest dust deposition the models disagree by more than two orders of magnitude. Aerosol at
21 Ragged Point was dominated by dust, sea-salt and soluble sulfates in varying proportions.
22 Contribution of sea-salt was dependent on local wind speed. Sulfate concentrations were linked to
23 long-range transport from Africa / Europe and South America / Southern Atlantic Ocean. Dust
24 sources were in Western Africa. The total dust deposition observed was $10 \text{ mg m}^{-2} \text{ d}^{-1}$ (range $0.5\text{--}47$
25 $\text{mg m}^{-2} \text{ d}^{-1}$), of which $0.67 \text{ mg m}^{-2} \text{ d}^{-1}$ was iron and $0.001 \text{ mg m}^{-2} \text{ d}^{-1}$ phosphorus. Iron deposition had
26 two sources, mainly silicate particles from Africa, and particularly in 2016 a lower contribution of
27 small iron-rich particles from South America or Barbados of probably anthropogenic origin. Dust
28 particles were mixed internally to a minor fraction (10 %), mostly with sea-salt and less frequently
29 with sulfate. It was estimated that average dust deposition velocity under ambient conditions is
30 increased by the internal mixture by 30–140 % for particles between 1 and $10 \mu\text{m}$ dust aerodynamic
31 diameter, with approximately 35 % at the mass median diameter of deposition ($7.0 \mu\text{m}$). For this size,
32 an effective deposition velocity of 6.4 mm/s (geometric standard deviation of 3.1 over all individual
33 particles) was observed.

34 **1 Introduction**

35 Mineral dust and sea-salt are globally the most abundant aerosol types in the atmosphere (Andreae
36 1995; Grini et al. 2005). They are considerably affecting the earth's radiation budget (Liao et al.
37 1998; Choobari et al. 2014) and have impact on cloud processes (Koehler et al. 2009; Tang et al.
38 2016; Karydis et al. 2017). Over the North Atlantic Ocean, large amounts of dust are transported
39 westwards in the Saharan Air Layer, until they reach the Caribbean (Karyampudi et al. 1999; Prospero
40 et al. 2014). Here, dust usually does not cross the Central American Dust Barrier (Nowottnick et al.
41 2011). Instead, it is down-mixed into the marine boundary layer by turbulent and convective
42 processes and removed from the atmosphere by wet and dry deposition processes. These processes
43 are not yet fully understood (Prospero et al. 2009; Nowottnick et al. 2011).



44 During its transport, mineral dust may undergo modifications by chemical processing, cloud
45 processing or microphysical effects (Andreae et al. 1986; Falkovich et al. 2001; Matsuki et al. 2005;
46 Sullivan et al. 2007a; Sullivan et al. 2007b). Different processes are expected to lead to different
47 modifications (e.g., Fitzgerald et al. 2015). These processes will change the composition and particle
48 size of dust, and thus modify its radiative properties and cloud impacts. To assess the mixing state of
49 mineral dust, techniques considering single particles are required. While there have been
50 investigations on dust mixing state in the past (Zhang et al. 1999; Zhang et al. 2004; Dall'Osto et al.
51 2010; Deboudt et al. 2010; Kandler et al. 2011a; Fitzgerald et al. 2015), the data basis is still limited.
52 In the present work, we present results from two field campaigns in summers 2013 and 2016, where
53 the aerosol in the marine boundary layer at Ragged Point in Barbados was collected by active and
54 passive sampling techniques.

55 A particular challenge for these campaigns was the high wind speed and the high humidities at the
56 sampling site. Therefore, the present publication consists of an extended methodical section with
57 three major topics and a methodical as well as atmosphere-related results section. One methodical
58 section deals with the determination of composition and mixing state of individual particles, taking
59 into account quantification artifacts and modeling the dust- and non-dust components as well as
60 their hygroscopic behavior. A second section is on particle collection representativeness and models
61 relating atmospheric concentration and deposition, taking into account the single particle properties
62 at ambient conditions. Finally, when aerosol mixing state is assessed based on offline aerosol
63 analysis, considerations on coincidental mixing have to be made to ensure the representativeness of
64 the results for the atmosphere. Therefore, in a third section these fundamental considerations based
65 on model as well as experimental data are presented. In the result section, we report first on these
66 theoretical and experimental methodical aspects, before we then discuss the atmospheric
67 implications of the measurements.

68 2 Methods

69 2.1 Particle sampling and location

70 Aerosol was sampled at Ragged Point, Barbados (13° 9' 54" N, 59° 25' 56" W) from June 14 until July
71 15, 2013, and from August 6 until August 28, 2016. Sampling was performed on top of the
72 measurement tower, approximately 17 m above the bluff (Zamora et al. 2011), which descends 30 m
73 to the sea surface. Particles were collected on pure carbon adhesive (Spectro Tabs, Plano GmbH,
74 Wetzlar, Germany) mounted on standard SEM aluminum stubs (Free-wing impactor, Dry particulate
75 deposition sampler) or pure nickel plates (cascade impactor).

76 2.1.1 Free-wing impactor (FWI)

77 A FWI was constructed for inlet-free collection of particles larger than 5 μm in diameter. A FWI
78 consists in general of a rotating arm with a sampling substrate attached, which acts as body impactor
79 (see Fig. S1 in electronic supplement). Rotation speed, wind speed and sample substrate geometry
80 determine the particle size cut-off for collection. FWI applied in previous investigations were
81 constructed with a rigid setup, so adaptation to actual meteorological conditions (i.e. perpendicular
82 adjustment of the impaction vector) needed to be performed by hand or was neglected (Jaenicke et
83 al. 1967; Noll 1970; Noll et al. 1985; Kandler et al. 2009). The present setup achieves perpendicularity
84 by self-adjustment of the flexibly mounted sampling substrate to the sum vector of wind and rotary
85 movement. This is performed by addition of a small wind vane at the rotating arm adjusting the angle



86 of the substrate. The rotating arm is driven by a stepper motor, which is mounted on a larger wind
87 vane, aligning the construction with the horizontal wind vector. To ensure that the wind vanes
88 respond only to the dynamic pressure, any imbalance in the setup must be avoided. The arm length
89 of the FWI is 0.25 m. With a constant rotation frequency of 10 Hz and the wind speeds at the
90 sampling location, particle impaction speeds between 16.4 and 20.2 m/s were achieved. This
91 corresponded to sampling volumes of air between 2.7 and 14.7 m³ for the present campaign. While
92 in principle the FWI could disturb its own flow field in low wind situations – the sample collector may
93 be influenced by its own wake from the previous rotation – this was not an issue for the present
94 work, as the distance of the sampling volume shifted by the wind between the same angular
95 positions of two consecutive rotations was always larger than 0.45 m. This is a large and therefore
96 safe distance in comparison to the small diameter of the sampling substrate and the counterweight
97 (12.5 mm and 25 mm, respectively). In total, 30 samples were collected during the campaign in 2013.

98 **2.1.2 Dry particulate deposition sampler (DPDS)**

99 The DPDS used in the present work is derived from the flat plate sampler of Ott et al. (2008b), which
100 performed best with respect to wind speed dependence in their tests. It consists of two round brass
101 plates (top plate diameter 203 mm, bottom plate 127 mm, thickness 1 mm each) mounted in a
102 distance of 16 mm. In contrast to the referred design, the one used here has a cylindrical dip in the
103 lower plate, which removes the sampling substrate – a SEM stub with a height of 3.2 mm – from the
104 airflow, reducing the flow disturbance. The dip is larger than the SEM stub and has small holes in the
105 bottom to catch and dispose droplets creeping across the lower plate due to the wind dynamical
106 pressure. The top surface of the SEM stub is located 5 mm below the lower plate's top surface.
107 Larger droplets (> 1 mm) are prevented by this setup from reaching the SEM stub surface at the local
108 wind speeds (Ott et al. 2008b). A total of 29 samples were collected in 2013 and 22 in 2016.

109 **2.1.3 Cascade impactor (CI)**

110 While the principle design of the used CI is described by Kandler et al. (2007), a new version with a
111 larger housing, but with the same collection characteristics, was deployed in the present work. An
112 omnidirectional inlet with a central flow deflector cone was used, whose transmission is discussed in
113 section 2.4.3. The impactor was operated at a flow rate of 0.48 l/min, which is set by a critical nozzle.
114 Nozzle diameters of 2.04, 1.31, 0.71, 0.49, 0.38, and 0.25 mm were used, corresponding to nominal
115 cut-off aerodynamic diameters of 5.2, 2.7, 1.0, 0.54, 0.33, and 0.1 μm, respectively. Sampling times
116 were adjusted to the estimated aerosol concentration and ranged between 10 and 60 min for the
117 supermicron and between 12 and 45 s for the submicron fraction. A total of 30 CI samples were
118 collected in 2013.

119 **2.2 Meteorological data, backward trajectory analyses and high-volume 120 sampling / mass concentrations**

121 In 2013, meteorological data was obtained at Ragged Point directly next to the particle sampling
122 devices. In 2016 wind, temperature and relative humidity were measured in parallel at The Barbados
123 Cloud Observatory at Deebles Point, which is located 400 m across a small cove to the southeast
124 (Stevens et al. 2016).

125 The measurements in 2013 are grouped into two time periods divided by the passage of the tropical
126 storm Chantal, which changed the atmospheric structure and air mass origin (Weinzierl et al. 2017).
127 The period from June 14 to July 8 will be referred to as pre-storm, the one from July 10 to 15 as post-
128 storm.



129 Backward trajectories were calculated with Hysplit 4 rev. 761 (Stein et al. 2015) based on Global Data
130 Assimilation System (GDAS) with 0.5 ° grid resolution (NOAA-ARL 2017). A backward-trajectory
131 ensemble consisting of a grid of 3x3 trajectories ending at 13.16483 (± 0.5)° N and 59.43203 (± 0.5) °
132 W at each altitude above sea level (300, 500, 700, 1000, 1500, and 2500 m) was calculated. Backward
133 trajectory length was 10 days in 1-hour steps, and an ensemble calculation was started for every
134 hour during the sample collection periods. Taking into account particle concentrations and
135 deposition rates as well as chemical properties, potential source contribution functions (PSCF) were
136 calculated (Ashbaugh et al. 1985) with a boundary layer approach. For each trajectory point it was
137 checked, whether the trajectory altitude was below the lowest boundary layer height provided by
138 the GDAS data set. If this condition was met, this particular point was regarded as a potential aerosol
139 injection spot and counted into the according source grid cell of 1° x 1° size. For determining possible
140 sources, all trajectories originating during collection of a particular sample were attributed with
141 sample properties of interest. Finally, the average for each source grid cell was calculated and then
142 weighted with a function based on the number of points in the cell to avoid an overrepresentation of
143 cells with high statistical uncertainty. The weighting function is generalized from the step function of
144 Xu et al. (2010) as

$$wt_{PSCF} = \exp \left[-2.93 \left(\frac{W_j}{\bar{W}} + 0.89 \right)^{-2.94} \right] \quad (1)$$

145 with W_j the number of trajectory points counted in cell number j ,
146 \bar{W} the average number of trajectory points per cell.

147 As result, a map based on PSCF shows regions with typically high or low values for airmasses passing
148 through the boundary layer in according grid cells. Note that by this approach, sources contributing
149 to advected aerosol can be identified, but local sources of course will not provide a usable signal.
150 Also, aerosol from remote sources might be transported inside the boundary layer and, thus, would
151 be attributed to also to the transport path in addition to its source.

152 **2.3 Scanning electron microscopy: individual particle composition,** 153 **analytical and statistical uncertainties**

154 About 22,000 individual particles (FWI), 65,700 (DPDS) and 26,500 (CI) were analyzed with a scanning
155 electron microscope (SEM; FEI ESEM Quanta 200 FEG and 400 FEG, FEI, Eindhoven, The Netherlands)
156 combined with an energy-dispersive X-ray analysis (EDX; EDAX Phoenix, EDAX, Tilburg, The
157 Netherlands and Oxford X-Max 120, Oxford Instruments, Abingdon, United Kingdom). The samples
158 were analyzed under vacuum conditions (approximately 10⁻² Pa) without any pretreatment. Before
159 automated analysis, samples were screened for surface defects, distinctive unusual particles shapes
160 or deposition patterns indicating possible artifacts or contamination, and traces of liquids. Areas with
161 surface defects (holes and bubbles in the substrate) were excluded from further data processing. The
162 remaining areas were free from artifacts. However, FWI samples suffered in general from the
163 presence of dried sea-spray droplets. Sample analysis was performed automatically by the software-
164 controlled electron microscope (software EDAX/AMETEK GENESIS 5.231 and Oxford Aztec 3.3).
165 Automated particle segmentation from the background was performed with the backscatter electron
166 signal. An acceleration voltage of 12.5 kV, a 'spot size 5' (beam diameter about 3 nm) and a working
167 distance of approximately 10 mm were used. Scanning resolution was adjusted to the particles size.
168 For the FWI and DPDS samples 140 to 300 nm/pixel were used, for the CI samples 180 or 360
169 nm/pixel for the stage containing the largest particles (mainly particles larger than 2.5 μm diameter)



170 and 73 nm/pixel for the stages containing smaller particles. An X-ray signal collection time between
171 15 s and 20 s (EDAX) and 2 s (Oxford) for each particle was used (yielding 40,000–100,000 total
172 counts), during which the beam was scanned over the particle cross section area.

173 The image analysis integrated into the SEM-EDX software determines the particles size as projected
174 area diameter:

$$d_g = \sqrt{4B/\pi} \quad (2)$$

175 with B the area covered by the particle on the sample substrate.

176 Following Ott et al. (2008a), the volume-equivalent diameter is estimated from the projected area
177 diameter via the volumetric shape factor expressed by particle projected area and perimeter as

$$d_v = \frac{4\pi B}{P^2} d_g = \frac{1}{P^2} \sqrt{64\pi B^3} \quad (3)$$

178 with P the perimeter of the particle.

179 In addition, for the assessment of particle coverage homogeneity and size distribution determination
180 series of 1,000 to 2,700 images were acquired for each sample. They were analyzed by the Software
181 Fiji/ImageJ 1.51d (Rasband 2015), using also Eq. (2) for particle size determination after application
182 of a “triangle” type auto threshold for particles segmentation (refer to Fiji/ImageJ documentation for
183 further details).

184 2.3.1 Quantification of elemental composition

185 Fully quantitative results in EDX analysis can only be reached under specific sample conditions. When
186 the composition of an analyzed spot is derived from an X-ray spectrum, the sample geometry has to
187 be considered. Besides assuming perfect smoothness and homogeneity, commonly either infinite
188 sample depth (i.e. significantly larger than the interaction volume of a few μm) or presence of an
189 infinitely thin film is assumed. In the former case, a ‘ZAF’ correction can be applied (Trincavelli et al.
190 2014), in the latter for example the Cliff-Lorimer method (Cliff et al. 1975). However, for particles
191 these assumptions and the resulting quantifications are not valid, as shown by Laskin et al. (2006) in
192 their Fig. 3. To overcome this problem, several standard-less techniques can be applied (Trincavelli et
193 al. 2014), for example a Monte Carlo simulation of the interaction volume can be used (Ro et al.
194 2003). Alternatively, particle ZAF algorithms can be applied at least for larger particles with diameters
195 above 1 μm (Armstrong 1991; Weinbruch et al. 1997). In the present work, however, an approach
196 with less computational cost is applied. First, on the measurement side, a lower acceleration
197 voltage—12.5 kV instead of 20 kV in comparative studies – eases the particle morphology problem.
198 Second, on the data analysis side by combining the above-mentioned correction methods as function
199 of particle size, a higher accuracy can be achieved. In principle, particle smaller than a limit size are
200 considered as thin films and particles large than a second limit are considered to be of infinite depth.
201 Between the limiting sizes, values are interpolated. To determine the best interpolation method,
202 samples with well-known composition (sodium chloride, albite) were milled to obtain particle
203 standards with sizes between 1 and 30 μm . Particles were dispersed in clean air, re-deposited on the
204 same sampling substrate and analyzed like described above. Several non-linear interpolation
205 schemes were tested; the best results were obtained with:



$$\langle X \rangle = \begin{cases} X_{CL} & d_g \leq d_l \\ X_{CL} + (X_{ZAF} - X_{CL}) \frac{\log(d_g/d_l)}{\log(d_u/d_l)} & d_l < d_g \leq d_u \\ X_{ZAF} & d_g > d_u \end{cases} \quad (4)$$

206 with $\langle X \rangle$ the corrected concentration of a particular element in the
 207 beam interaction volume,

208 X_{CL} the element concentration determined by the Cliff-Lorrimer method,

209 X_{ZAF} the element concentration determined by the ZAF method,

210 $d_l = 1.5 \mu\text{m}$ the lower interpolation range size limit,

211 $d_u = 30 \mu\text{m}$ the upper interpolation range size limit.

212 Note that the concentrations are always normalized to 100 % of the beam interaction volume, which
 213 can include besides the particle also the substrate; i.e. they do only indirectly represent an amount of
 214 matter with respect to the particle. The correction is identical for atomic and mass concentrations; in
 215 the present manuscript, atomic concentrations are used unless otherwise specified.

216 The result of the correction as function of particle size is shown in Fig. 1. It becomes clearly visible
 217 that the accuracy of the quantification is strongly improved, while the major uncertainty remaining
 218 originates from the particle to particle variation. This uncertainty depends on the noise in the
 219 analysis system, but is also related to particle surface morphology and its variability. The latter
 220 affects the X-ray signal mainly by unknown absorption path lengths, particularly for the lighter
 221 elements, as illustrated by Fletcher et al. (2011). The measurements shown here were performed at
 222 20 kV acceleration voltage; at 12.5 kV as used for the sample analyses, the problems are considerably
 223 less pronounced.

224 Application to a sample of atmospheric particles is shown in Fig. 2. Particles dominated by Na and Cl
 225 were selected from all DPDS samples, and the positive and negative ion contributions were
 226 calculated for each particle from the determined concentration. It becomes obvious, that for a wide
 227 size range the applied correction works well and produces therefore unbiased relative
 228 concentrations for the considered elements. The outliers may occur due to noise, the negligence of
 229 C, N and O compounds or an internal mixture of sea-salt with dust (e.g., NaAlSi₃O₈, FeS).

230 Using the measured and corrected atomic concentrations, an element index is defined as:

$$|X_i| = \frac{\langle X_i \rangle}{\sum \langle X \rangle} \quad (5)$$

231 with $|X_i|$ element index of a particular element with arbitrary index i ,

232 $\sum \langle X \rangle$ sum of all considered elements (Na, Mg, Al, Si, P, S, Cl, K, Ca, Ti, Cr, Mn, Fe, Co,
 233 if not stated differently).

234 2.3.2 Analytical measurement errors

235 A typical deposition sample (collected between June 21, 2013, 13:46 and June 22, 15:02, local time)
 236 was analyzed 29 times with a signal collection time per particle of 16 s. The same 300 particles were
 237 analyzed each time. For illustration of the typical precision, the particles consisting mainly of Na and
 238 Cl were selected from. Fig. 3 illustrates the average composition and standard deviation (1σ) for
 239 each particle. The average values show a typical behavior for atmospheric sea-salt with a slightly
 240 depleted Cl and enriched S concentration (e.g., McInnes et al. 1994). The precision – shown as
 241 relative standard deviation – increases with particle size. This is caused by the increasing amount of



242 material contributing to the particle's signal up to a point at about 3 μm particles, from which the
243 beam excitation volume is completely inside the particle. For the major compounds, the precision is
244 in the range of 2 % relative standard deviation. For minor compounds, it is between 10 and 20 % for
245 particles 3 μm and larger, but can exceed 100 % for the smallest ones. The latter high uncertainties
246 could be decreased with suitable working conditions (magnification, measurement time), but are not
247 focus of the present paper.

248 The uncertainty in particle diameter also depends on its size. For particles with 2 μm diameter, the
249 relative standard deviation is about 1.5 % decreasing to less than 1 % for particles larger than 3 μm .
250 This is in the same range as the systematic accuracy of SEM (1–2 %).

251 **2.3.3 Estimation of the dust contribution to each single particle in a dust / sea-salt /** 252 **sulfate mixture and the size of the according dust inclusion**

253 Sampling was performed in a region where locally emitted sea-salt aerosol and other soluble species
254 are mixed with long-range transported mineral dust. As in particular the mineral dust contribution is
255 of special interest, dis-entangling the particle populations and considering them separately an
256 important task.

257 To calculate the size of a dust inclusion and the according volume fraction for an internally mixed
258 particle from the chemical composition, the different elemental contributions have to be attributed
259 to the dust or non-dust component. This analysis is restricted in the present work to the major
260 compounds only. For Al, Si, P, Ti and Fe it can be safely assumed that they belong to the dust
261 component, and S and Cl can be attributed to the non-dust component. Na, Mg, K and Ca, however,
262 are ambiguous and can be present in fractions. Therefore, a model is needed to estimate the
263 contribution of the ambiguous elements from the dust and non-dust component based on the single
264 particle chemical composition.

265 A problem arises here from the error in chemical quantification due to matrix composition and
266 particle geometry. While the correction outlined in section 2.3.1 adjusts the quantification accuracy
267 of the average particle composition, for single particles because of their unknown geometry and
268 surface orientation angles, still a considerable error in element quantification can occur. In particular,
269 a bias between light and heavier elements can be introduced by unaccounted X-ray absorption,
270 which can lead to under- as well as overestimation of the relative contribution of light elements
271 (Fletcher et al. 2011). As for the present aerosol the major cations (Na^+ , Mg^{2+}) are light in comparison
272 to the major anions (Cl^- , S of SO_4^{2-}), a quantification bias will lead to an error in component
273 attribution. Particularly, an overestimation of the light elements will yield – by attribution of the ion
274 balance excess to the dust component – to an overestimation of the dust contribution. Therefore,
275 two model pathways are applied: an upper limit estimate, where a possibly overestimated fraction of
276 the ambiguous elements is attributed to the dust component, and a lower limit estimate, where all
277 ambiguous elements are attributed to the non-dust component.

278 The following assumptions are made:

- 279 1. There is exactly one dust inclusion in each mixed particle
- 280 2. Carbonaceous matter does not contribute
- 281 3. Ca contributes to dust as carbonate
- 282 4. Ca contributes to non-dust as sulfate / chloride
- 283 5. Fe contributes to dust as Fe^{3+}
- 284 6. S contributes as sulfate



- 285 7. Na, Mg, Al, Si, P, K, Ti and Fe contribute to the dust according to their oxide weights
 286 8. N-containing compounds contribute only in case of a non-neutral ion balance as ammonium
 287 and nitrate
 288 9. Dust density is $\rho_{dust} = 2650 \frac{kg}{m^3}$, non-dust density is $\rho_{nondust} = 2200 \frac{kg}{m^3}$, averaged from
 289 typical dust and non-dust constituents: illite, kaolinite, muscovite, quartz, albite, microcline,
 290 calcite, gypsum, halite, sodium sulfate minerals in different hydration states, and
 291 mascagnite (Deer et al. 1992; Warneck et al. 2012)

292 **Estimation of the upper limit**

293 Following the above-listed assumptions, the apparent cation/anion charge ratio is defined as

$$r_{cat} = \frac{\sum cations_{charge}}{\sum anions_{charge}} \quad (6)$$

294 with $\sum cations_{charge} = |Na| + 2|Mg| + |K| + 2|Ca|$, apparent sum of cation charges,

295 and $\sum anions_{charge} = |Cl| + 2|S|$, apparent sum of anion charges.

296 Note that $|X|$ denominates the concentration of element $\langle X \rangle$ given as atomic (i.e. molar) fraction
 297 relative to the sum of all quantified element concentrations with the exclusion of O and lighter
 298 elements.

299 If $r_{cat} > 1$, it is assumed in the upper limit estimate that the excess in the apparent sum of cation
 300 charges is produced by the dust contribution. Thus, the dust contribution is calculated as the ion
 301 balance excess as

$$c_{dust} = \frac{r_{cat} - 1}{r_{cat}} = \frac{\frac{\sum cations_{charge}}{\sum anions_{charge}} - 1}{\frac{\sum cations_{charge}}{\sum anions_{charge}}} = \frac{\sum cations_{charge} - \sum anions_{charge}}{\sum cations_{charge}} \quad (7)$$

302 Cation excess

303 If $c_{dust} > 0$, an equal fraction of each element's apparent cation contribution excess is attributed to
 304 dust, i.e. the ion charge balance is virtually neutralized for the non-dust component. The dust and
 305 non-dust masses are calculated as (see also Table S1 in electronic supplement)

$$m_{dust} = \sum dust_{oxides} + c_{dust} \sum cations_{oxide} \quad (8)$$

306 with $\sum dust_{oxides} = Al_{oxide} + Si_{oxide} + P_{oxide} + Ti_{oxide} + Fe_{oxide}$,

307 and $\sum cations_{oxide} = Na_{oxide} + Mg_{oxide} + K_{oxide} + Ca_{carbonate}$.

308 Note that stable sulfates (gypsum / anhydrite, alunite) are assigned to the non-dust component.

$$m_{nondust} = (1 - c_{dust}) \sum cations_{mass} + \sum anions_{mass} \quad (9)$$

309

310 with $\sum cations_{mass} = Na_{mass} + Mg_{mass} + K_{mass} + Ca_{mass}$,

311 and $\sum anions_{mass} = Cl_{mass} + SO_{4, mass}^{2-}$.

312 The mass contributions are calculated as shown in Table S1 in the electronic supplement.



313 Cation deficit

314 If $c_{dust} < 0$, i.e. there is a cation deficit, the missing cation is assumed to be ammonium. The dust

315 and non-dust masses are then calculated as

$$m_{dust} = \sum oxides \quad (10)$$

$$m_{nondust} = \sum cations_{mass} + \sum anions_{mass} + NH_{4,mass}^+ \quad (11)$$

316 For calculation of the ammonium mass $NH_{4,mass}^+$ see Table S1 in the electronic supplement.

317 **Estimation of the lower limit**

318 The dust mass for lower limit estimate of the dust contribution is calculated according to Eq. (10).

319 The non-dust mass is calculated for $c_{dust} < 0$ according to Eq. (11). For $c_{dust} > 0$ nitrate is assumed

320 to be the missing anion and the non-dust mass is calculated as

$$m_{nondust} = \sum cations_{mass} + \sum anions_{mass} + NO_{3,mass}^- \quad (12)$$

321 Refer to Table S1 in the electronic supplement for calculation of the nitrate mass.

322 **Calculation of the dust fraction**

323 From the dust and non-dust mass contributions, the dust volume contribution to the particle is

324 calculated as

$$f_{dust} = \frac{\frac{m_{dust}}{\rho_{dust}}}{\frac{m_{dust}}{\rho_{dust}} + \frac{m_{nondust}}{\rho_{nondust}}} = \frac{m_{dust}}{m_{dust} + \frac{\rho_{dust}}{\rho_{nondust}} m_{nondust}} \quad (13)$$

325

326 and the diameter of the resulting dust inclusion as

$$\frac{\pi}{6} d_{v,dust}^3 = f_{dust} \frac{\pi}{6} d_v^3 \rightarrow d_{v,dust} = f_{dust}^{\frac{1}{3}} d_v \quad (14)$$

327

328 The model outlined here by suffer from systematic errors:

329 1. In the presence of larger amount of nitrate and ammonium or organics, the dust contribution will

330 be overestimated, as the regarded composition is fitted to the apparent particle volume. However, in

331 Barbados the concentration of these compounds is usually small in comparison to the dust (Lepple et

332 al. 1976; Savoie et al. 1992; Eglinton et al. 2002; Prospero et al. 2009; Zamora et al. 2011).

333 2. The density values are averages for the assumed components, and the real density of a particle

334 may be smaller or larger. However, the density range for the components in question is small (dust:

335 2300 to 3000 kg/m³, non-dust 1800 to 2600 kg/m³ at maximum), so the error is considered to be less

336 than 10 %.

337 3. The mass contribution is estimated by ion charge balances. If for the ambiguous elements an

338 inhomogeneous distribution of univalent and bivalent elements exists (e.g., univalent like Na favoring

339 the non-dust component and bivalent like Ca favoring the dust component), an error of less than 5 %

340 in diameter can occur. With an assumption of 5 % iron content in dust, the maximum error due to

341 the Fe³⁺ assumption is less than 0.2 % in diameter.



342 The upper and lower estimates yield diameters, which differ for the dust core diameter in average by
343 25 %; for 75 % of the particles the difference is less than a factor of two. From the analytical errors in
344 ratios for major compounds (less than 10 % systematically and 6 % repetition uncertainty), an dust
345 core size uncertainty of about 6 % is estimated, as long as the core is larger than 10 % of the particle.
346 An overall analytical uncertainty of 15 % relative core size is estimated. In conjunction with the
347 upper/lower limit estimates, an overall core size error of 25 % is considered appropriate.

348 ***Estimation of a geometrical iron-availability index***

349 Iron bioavailability in general is depending on different chemical and microphysical parameters as
350 well as residence time in chemically aggressive environments (Shi et al. 2011a; Shi et al. 2012). If
351 considering a homogeneous iron distribution in larger and smaller particles, it seems plausible that
352 the distance to the surface – therefore the surface to volume ratio – should have an impact on the
353 short-term iron accessibility (e.g., Baker et al. 2006; Shi et al. 2011b). Therefore, as first order
354 estimate we define a geometrical surface iron availability index SIAI (after virtual dissolution of the
355 soluble compounds) as

$$SIAI = \frac{Fe_{oxide}}{m_{dust}} 4\pi d_{v,dust}^2 \quad (15)$$

356 **2.3.4 Particle classification and relative ion balance**

357 For assessing the abundances and counting statistics of certain particle types, the particles were
358 classified into different groups and classes. Based on the element index and additional elemental
359 ratios, a set of rules used in former mineral dust investigations in a marine environment was applied
360 therefore. For details refer to Kandler et al. (2011a).

361 In addition, a relative ion balance is defined for single particles as:

$$IB_{rel} = \frac{\langle Na \rangle + 2\langle Mg \rangle + \langle K \rangle + 2\langle Ca \rangle - \langle Cl \rangle - 2\langle S \rangle}{\langle Na \rangle + 2\langle Mg \rangle + \langle K \rangle + 2\langle Ca \rangle + \langle Cl \rangle + 2\langle S \rangle} \quad (16)$$

362 A positive relative ion balance – i.e. an excess of positive ions – would indicate an undetected
363 presence of negative ions like NO_3^- or CO_3^{2-} , a negative one such of H^+ or NH_3^+ , which all can't be
364 (reliably) quantified by EDX. The relative ion balance is calculated only for particles classified into the
365 soluble sulfate or sea-salt classes (see below for classification scheme).

366 **2.3.5 Statistical uncertainty of total volumes / masses and relative number abundances 367 from single particle measurements**

368 When assessing the uncertainty of values based on counted occurrences, frequently the counting
369 statistics are assumed to follow a Poisson distribution. However, when calculating total aerosol
370 masses or volumes, besides the measurement errors in particular the – usually few – large particles
371 can introduce a considerable statistical uncertainty, which is not necessarily accounted for by the
372 distribution assumption. Therefore, estimates of the statistical uncertainty based on single particle
373 counts for an a priori unknown frequency distribution (i. e. the counting frequency distribution
374 modified by the also unknown particle size distribution) either require reasonable assumptions or
375 distribution-independent estimators. In the present work, the uncertainty is estimated by a
376 bootstrap approach with Monte Carlo approximation (Efron 1979). Furthermore, the results of the
377 generally robust bootstrap approach (Efron 2003) are compared to a more simple approach, where
378 the counting statistics is assumed to follow a Poisson distribution. The Gaussian error propagation is
379 then calculated for the latter case.



380 For the bootstrap approach, a considerable number of data replications are necessary (Carpenter et
381 al. 2000; Pattengale et al. 2010). On the actual number, different recommendations exist with more
382 than 1000 being among the most common (Carpenter et al. 2000). As higher numbers lead to smaller
383 errors in the uncertainty estimate, 10,000 replications for each sample were performed in the
384 present work.

385 For the Poisson approach, with a counting error of $\Delta n = 1$ for a single particle count ($n = 1$) the
386 Gaussian error propagation of the standard deviation for a sum of particle volumes V_k resolves to

$$\Delta V = \sqrt{\sum_k \left(\Delta n \frac{\partial}{\partial n} n V_k \right)^2 + \sum_k \left(\Delta V_k \frac{\partial}{\partial V_k} n V_k \right)^2} = \sqrt{\sum_k V_k^2 + \sum_k \Delta V_k^2} \quad (17)$$

387 with n the number of particles with Volume V_k , in this case always 1,
388 ΔV_k the volume measurement error,
389 k the index for the single particles.

390 Similar considerations apply for the mass calculations.

391 The two-sided 95 % confidence interval is estimated for the Poisson distribution case as 1.96 times
392 the standard deviation, and for the bootstrap case as the 0.025 to 0.975 quantile range of the
393 bootstrap replications (bias corrected and accelerated method; DiCiccio et al. 1996; Carpenter et al.
394 2000).

395 Considering only the statistical uncertainty from Eq. (17), the distribution-based approach can be
396 compared to the bootstrap approach in terms of relative statistical uncertainty for the volume
397 estimated from two methods (Fig. 4). Clearly, the Poisson assumption underestimates the lower limit
398 of the two-sided 95 % confidence interval (i.e. overestimates the uncertainty), providing even
399 physically meaningless negative numbers. In contrast, the bootstrap approach yields most probably
400 more precise estimates (see also Efron 2003). For the upper limit of the interval, the Poisson
401 approach seems to underestimate the uncertainty, in particular with respect to the high volumes
402 which can be present in single particles (Fig. 4, left). When restricting the size range to particles of 1
403 μm to 20 μm in diameter (Fig. 4, right), as expected the differences in confidence interval limits
404 become much smaller and stay mostly below 20 % difference between the two approaches. Note in
405 particular the impact of the volume in the single largest particle. For the present work, the bootstrap
406 approach is preferred.

407 For the assessment of the confidence interval of relative counting abundances, frequently a
408 confidence interval based on a binomial distribution is used as estimate (Agestri et al. 1998), i.e. for a
409 relative number abundance of a certain particle type class r the two-sided 95 % confidence interval is
410 approximated as (Hartung et al. 2005)

$$CL_{0.025,0.975} = \frac{3.84 + 2r \mp \sqrt{3.84 \left(3.84 + 4r \frac{n-r}{n} \right)}}{2(n + 3.84)} \quad (18)$$

411 with r the count of particles in that class,
412 n the total number of particles.

413 The two approaches show much closer agreement here than in the previous case (see Fig. S2 in
414 electronic supplement). Note that if the common Wald confidence interval is used (Agestri et al.



415 1998), with lower absolute particle numbers in a class, an increasing tendency of
 416 over/underestimation similar to the previous case occurs up to meaningless negative values in the
 417 binomial case. For sake of consistence, in the present work also for the relative abundances the
 418 robust bootstrap approach for estimation of the confidence intervals was chosen.

419 **2.4 Collection efficiency and deposition velocity relating atmospheric** 420 **concentrations to deposition rates**

421 **2.4.1 Determining the size distributions from the free-wing impactor measurements**

422 Obtaining the atmospheric size distribution and representative contributions of particle populations
 423 with different hygroscopicity from the FWI requires a set of corrections. These corrections are
 424 applied to each single particle as a function of its size and composition and the thermodynamic
 425 conditions during sampling by weighting its count with the product of all correction functions. First, a
 426 window correction accounting for the exclusion of particles at the analysis image border is applied
 427 (Kandler et al. 2009):

$$c_w = \frac{w_x w_y}{(w_x - d_p)(w_y - d_p)} \quad (19)$$

428 Second, the collection efficiency of the FWI has to be regarded. Therefore, the ambient particle
 429 diameter at the time of collection has to be estimated by accounting for the hygroscopic particle
 430 growth:

$$d_{amb} = d_v g_{hyg} \quad (20)$$

431 with g_{hyg} the hygroscopic growth factor.

432 Hygroscopic growth can be estimated from the hygroscopicity parameter κ (Petters et al. 2007) as

$$g_{hyg} = \left(1 + \frac{a_w}{1 - a_w} \kappa\right)^{\frac{1}{3}} \quad (21)$$

433 with a_w the water activity.

434 As only super-micron particles are considered in this part of the study, the water activity can be
 435 equated with the relative humidity given as fraction. The hygroscopicity parameter can be
 436 determined as volume-weighted average of the hygroscopicity parameters of the major contributing
 437 components (Petters et al. 2007). Assuming a mixture of sodium sulfate and sodium chloride as the
 438 components dominating the hygroscopic growth and assigning the dust component zero
 439 hygroscopicity, the hygroscopicity parameter is approximated from the volume contributions as

$$\kappa = (1 - f_{dust}) \frac{0.68 \times Na_2SO_{4,volume} + 1.12 \times NaCl_{volume}}{Na_2SO_{4,volume} + NaCl_{volume}} \quad (22)$$

440 For the calculation of the volume contributions, refer to Table S1 in the electronic supplement.

441 The collection efficiency $E(P)$ is parameterized (see below) from the experimentally determined
 442 values for discs given by May et al. (1967) as a function of impaction parameter P :

$$P = \frac{S}{D} \quad (23)$$



443 with S stopping distance,
 444 D characteristic dimension, here 12.5 mm.

445 While P equals to the Stokes number within the Stokes regime, in the current work the particle
 446 Reynolds numbers are considerably higher. In this regime, in analogy to Hinds (1999) the stopping
 447 distance can be approximated with better than 3 % accuracy as

$$S = \frac{\rho_{amb} d_{amb}}{\rho_a \sqrt{\chi}} \left[Re_p^{\frac{1}{3}} - \sqrt{6} \tan^{-1} \left(\frac{Re_p^{\frac{1}{3}}}{\sqrt{6}} \right) \right] \quad (24)$$

448 with ρ_{amb} ambient particle density, estimated from chemical composition and growth factor,
 449 ρ_a air density,
 450 χ aerodynamic shape factor.

451 Results of the trigonometric function must be given as radian. The dry aerodynamic shape factor is
 452 assumed as constant similar to Ott et al. (2008a), but is interpolated for particles mixed with water as
 453 function of the hygroscopic growth factor:

$$\chi = \begin{cases} 1 + (\chi_0 - 1) \left(1 - \frac{g_{hyg} - 1}{g_{hyg,lim}} \right) & g_{hyg} < g_{hyg,lim} \\ 1 & g_{hyg} > g_{hyg,lim} \end{cases} \quad (25)$$

454 with $\chi_0 = 1.4$ an estimated dry shape factor (Ott et al. 2008a)
 455 $g_{hyg,lim} = 1.3$ a hygroscopic growth factor at which the particles are assumed to be
 456 spherical.

457 The particle Reynolds number is

$$Re_p = \frac{\rho_a v_i d_{amb}}{\eta \sqrt{\chi}} \quad (26)$$

458 with $v_i = \sqrt{v_r^2 + v^2}$ the impaction velocity
 459 $v_r = 2\pi l f_r$ the speed of the collector in the plane of rotation
 460 l the collector arm length
 461 f_r the rotation frequency
 462 v the wind speed
 463 η the viscosity of the air.

464 The stopping distances calculated by Eq. (24) are well in accordance with the parameterization
 465 curves shown by May et al. (1967).

466 The collection $E(P)$ efficiency for $P > 0.125$ is then parameterized (see Fig. S3 in the electronic
 467 supplement) and the according correction is

$$c_e = \frac{1}{E(P)} = \exp\left(\frac{0.28}{P}\right) \quad (27)$$

468 The total investigated volume for the concentration calculations is determined by

$$V_i = A v_i t_i \quad (28)$$



469 with A the analyzed area,
 470 t_i the sample collection time.

471 The atmospheric concentration is finally

$$C(d_{amb}) = \frac{1}{V_i} \sum_k c_w(d_{p,k}) c_e(d_{amb,k}) \quad (29)$$

472 with k index of the particle.

473 Potential systematic error sources for this calculation are mainly the uncertainty in collection
 474 efficiency, given the considerable spread in data points in the according literature (Golovin et al.
 475 1962; May et al. 1967), and any bias in particle size.

476 2.4.2 Determining the airborne size distributions from the sedimentation sampler 477 measurements

478 Similar to the previous section, sampling efficiency considerations are necessary for the
 479 sedimentation sampler. For the supermicron particle size range sedimentation and turbulent
 480 impaction dominate the particle deposition velocity (as for example illustrated by Piskunov 2009). To
 481 calculate the turbulent impaction velocity, which depends of the wind speed, the friction velocity is
 482 needed. As the opposing inner boundary layers of the sampler plates are always separated for the
 483 considered range of wind speeds (boundary layer thickness between 4.5 mm and 2 mm for wind
 484 speeds between 3.5 m/s and 13.5 m/s; Munson et al. 2013), the flow inside the sampler is
 485 approximated as flow over a smooth flat plate (the lower plate). The friction velocity is calculated as
 486 recommended by Wood (1981):

$$u^* = \frac{v}{\sqrt{2}} (2 \log_{10} Re_s - 0.65)^{-1.15} \quad (30)$$

487 with $Re_s = \frac{\rho_a v x}{\eta}$ the flow Reynolds number at the sampling stub location,
 488 x the distance from the lower plate edge to the center of the sampling stub
 489 (6.3 cm).

490 Considering the flow inside the sampler as tube flow (Liu et al. 1974) would lead to friction velocities
 491 differing by less than 5 %.

492 A variety of models estimating the particles deposition speed were published (Sehmel 1973; Slinn et
 493 al. 1980; Noll et al. 2001; Wagner et al. 2001; Aluko et al. 2006; Piskunov 2009; Petroff et al. 2010).
 494 They yield considerable different results, possibly due to negligence of unaccounted forces (e.g., Lai
 495 et al. 2005), the way of determining the relevant friction velocity, or other model assumptions. For
 496 the present work, the formalism of Piskunov (2009) was selected, as it derives the deposition velocity
 497 rather from physical principles instead of parameterizing a specific measurement setup. The
 498 deposition velocity is estimated by the following formalism:

$$v_d = \frac{u^*}{J_1 + J_2} \quad (31)$$

$$J_1 = \frac{u^* \exp(-1.2\tau^+)}{v_{stk}} \left[1 - \exp\left(-13.204 Sc^{\frac{2}{3}} \frac{v_{stk}}{u^*}\right) \right] \quad (32)$$



499 with $Sc = \frac{\eta}{\rho_a c_D} = \frac{3\pi \eta^2 d_{amb}}{\rho_a k_B T C_c \sqrt{\chi}}$ the Schmidt number,
 500 C_D the particle diffusion coefficient,
 501 k_B the Boltzmann constant,
 502 T the ambient temperature,
 503 $C_c = 1 + 2 \frac{\lambda \sqrt{\chi}}{d_{amb}} \left[1.257 + 0.4 \exp\left(-\frac{1.1 d_{amb}}{2\lambda \sqrt{\chi}}\right) \right]$ the Cunningham slip correction,
 504 $\lambda = \frac{k_B T}{\sqrt{2} \pi d_M^2 P}$ the mean free path,
 505 $d_M = 3.68 \times 10^{-10}$ m the average diameter of an air
 506 molecule,
 507 P the ambient pressure,
 508 $v_{Stk} = \frac{12 \eta \sqrt{\chi}}{0.42 C_c \rho_a d_{amb}} \left[\sqrt{1 + \frac{0.42 C_c^2 \rho_a \rho_{amb}}{108 \eta^2} \left(\frac{d_{amb}}{\sqrt{\chi}}\right)^3 \left(1 - \frac{\rho_a}{\rho_{amb}}\right) g} - 1 \right]$ the gravitational settling velocity,
 509 g the gravitational acceleration;
 510 $J_2 = \frac{1 - \exp\left[-\gamma \left(1 + \frac{v_{Stk}}{u^* p_\tau}\right)\right]}{p_\tau + \frac{v_{Stk}}{u^*}}$ (33)

511 with $\gamma = \frac{0.4611 Sc \tau^+ (1+0.3859 \tau^+)}{(1+0.1193 \tau^+)(1+0.1193 \tau^+ + 6.613 Sc)}$
 512 $\tau^+ = \frac{u^{*2} \rho_a v_{Stk}}{\eta g}$ the dimensionless relaxation time,
 513 $p_\tau = \frac{\tau^+ (1+0.3859 \tau^+)}{65.06 (1+0.1193 \tau^+)^2}$

514 The atmospheric concentrations are then

$$C(d_{amb}) = \frac{1}{A t_i} \sum_k \frac{c_w(d_{p,k})}{v_d(d_{amb,k})} \quad (34)$$

515 A major bias for this calculation originates from the uncertainty in (turbulent) deposition velocity.

516 The deposition velocity calculated by different formalisms for a series of deposition samples is shown
 517 in Fig. 5. The aerodynamic diameter used here is calculated as:

$$d_a = \sqrt{\frac{\rho_{amb}}{\rho_0 \chi}} d_{amb} \quad (35)$$

518 with $\rho_0 = 1000 \frac{\text{kg}}{\text{m}^3}$ unity density.

519 The spread in deposition velocity for each model is caused mainly by the different wind speeds
 520 during exposure, but also by the variation in relative humidity and, to a lesser extent, by other
 521 thermodynamic conditions. However, it becomes strikingly obvious that in the size range where most
 522 of the atmospheric dust deposition occurs – i.e. between 2 and 50 μm in diameter at Barbados
 523 (Mahowald et al. 2014; van der Does et al. 2016) –, the models disagree by more than two orders of
 524 magnitude. Besides the uncertainty derived from selection of a particular model, the sphericity
 525 assumption and the related drag effects may lead to a bias in deposition flux, most probably mainly
 526 influencing the turbulent deposition regime around 10 μm particle diameter. An additional
 527 measurement bias might be introduced by the parallelism assumption underlying all the stable
 528 boundary layer calculations, i. e. that the air flow must be parallel to the plate. While the vertical



529 component of the wind speed under atmospheric conditions is usually small in comparison to the
530 horizontal ones, still 'inlet' losses might occur even due to small non-parallel components. These inlet
531 losses are expected to affect mainly the largest particles sizes.

532 **2.4.3 Impactor inlets**

533 The impactor sampler was used with two types of inlets. For particles larger than approximately 2.5
534 μm aerodynamic diameter, a pseudo-isoaxial inlet orientation with sub-isokinetic sampling was used.
535 Smaller particles were collected with an omnidirectional inlet. As particles were analyzed separately
536 for each size class, the inlet efficiency does not play a primary role for the results, still it must be
537 considered. Literature on an accurate estimation of inlet transmission for a ratio between ambient
538 wind speed and impactor inlet flow velocity in the range of 100:1 is not existing. However, from Paik
539 et al. (2002) and Hangal et al. (1990) in conjunction with the observation of Li et al. (2002) regarding
540 the applicability of thin walled nozzle formulas to blunt samplers, it may be conclude that:

541 a) particles larger than 2.5 μm aerodynamic diameter would be increasingly enriched with increasing
542 particle sizes. Enrichment factors for thin-walled nozzles would be in the range of 2–4 for 10 μm
543 particles and 20–50 for 100 μm particles. As the sampler had a blunt inlet, the actual enrichment
544 factors are probably considerably lower.

545 b) particles smaller than 2.5 μm would be comparatively unbiased at low Stokes numbers; see also
546 Wen et al. (2000).

547 For a dry aerosol, these size-selective inlet losses would not considerably bias the relative chemical
548 composition. In the present humid environment with partly soluble species, though, it can lead to an
549 overestimation of non-hygroscopic species for particle sizes in the vicinity of the inlet cut-off, if the
550 hygroscopic growth is not explicitly considered. The problem is somewhat diminished by the fact that
551 by water-absorption the density of the particles decreases and, consequently, the Stokes number
552 increases only sub-proportionally to the square of the particle diameter. Nevertheless, the
553 hygroscopic growth should be explicitly accounted for. Therefore, the model from Eq. (20) is applied
554 based on the measured geometric diameter and chemical composition, and ambient chemical
555 compositions are computed.

556 **2.5 Modelling deposition statistics and artifacts of mixing state**

557 When particles are deposited to a substrate, they might touch each other and form an internal
558 mixture, which is not representative for the atmosphere. While the lower limit of coincidental
559 internal particle mixture on a substrate is easily defined – it equals the ratio of the area covered by
560 particles to the total analyses area for an infinitesimally small depositing particle – the assessment is
561 much more complex for larger particles following a wide size distribution function.

562 Therefore, in the first step the deposition process was simulated by a series of Monte Carlo models.
563 For input, the average size distribution measured at Cape Verde (Kandler et al. 2011b) – hereafter
564 CV-ground – and the median one measured airborne for aged dust (Weinzierl et al. 2011) – hereafter
565 CV-air – were used. These size distributions mainly differ in the concentration of supermicron
566 particles. The deposition velocity formulation after Piskunov (2009) was used. The modeled
567 deposition area is 5 mm x 5 mm, meteorological conditions were assumed as totally dry, 20 °C, sea
568 level pressure and a friction velocity of 0.2 m/s. Particles were virtually dropped onto the deposition
569 surface until either a certain fractional area coverage by particles or a simulated deposition time limit
570 was reached. Eighteen different area coverages were simulated for a two-component external



571 mixture (particle density 2200 kg/m^3) with components number ratios of 50 % / 50 %, 75 % / 25 %, 90
572 % / 10 %, 95 % / 5 %, 97 % / 3 %, and 99 % / 1 % for CV-ground, and nine area coverages with number
573 ratios of 50 % / 50%, 90 % / 10 %, and 99 % / 1 % for CV-air. Each model was run 1000 times (200
574 times in case of 0.1 and larger fraction area coverages) to assess the statistical uncertainty. In a
575 second series, for CV-ground a tri-component external mixture of sodium sulfate (particle density
576 1770 kg/m^3), dust (2700 kg/m^3) and sea-salt (2170 kg/m^3) was used as input. The size-dependent
577 component number contributions were taken from measurements at Cape Verde (Schladitz et al.
578 2011). After the simulated deposition, particle agglomerates on the substrate with touching contours
579 were merged into a new particle with the sum of the volumes and proportionate chemical
580 composition.

581 To investigate the relevance of mixing artifacts caused by particle sampling, the sensitivity of
582 SEM/EDX analysis has to be considered. Internal mixtures can be only detected by SEM/EDX, if the
583 minor component exceeds the limit of detection. At an acceleration voltage of 12.5 kV the primary X-
584 ray excitation volume is in the range of $0.5 \mu\text{m}$ to $1.5 \mu\text{m}$ diameter, depending on the matrix
585 elements (Goldstein et al. 2003). As we consider mainly supermicron particles, the excitation volume
586 is expected to be mainly inside the particles. According to our experience an X-ray peak becomes
587 detectable at about 0.3 % concentration. Therefore, a 1 % contribution of an element to the particle
588 volume will be definitely detectable. Thus, a particle containing more than 1 % material from another
589 particle type is considered as detectable mixture in the model. A particle containing more than 20 %
590 is denominated as strong internal mixture. Note that for smaller particles, when the excitation
591 volume would extend into the substrate, larger contributions to the particle volume would be
592 required.

593 Besides these fundamental considerations, in the second step a mixing model was applied to each
594 sample, based on its measured composition. Random particles were virtually selected from the pure
595 components of the measured set of particles and placed at random positions inside a virtual area
596 with the same size as the one analyzed in SEM/EDX, until the same area coverage as of the real
597 sample was reached. Internal mixtures artificially produced on the substrate were counted, if their
598 mixing would have been detected by SEM/EDX applying the rules for mixed particle classification.
599 This process was repeated 10,000 times. The upper 95 % confidence interval limit of mixtures
600 modeled by the Monte Carlo simulation was considered as limit of detection for internal mixtures,
601 and the median of the produced mixtures was regarded as systematic error and was subtracted from
602 the mixtures detected in the real samples.

603 In the third step, the single mixing probability (SMP) for each binary pure compound combination
604 was calculated by selecting 100,000 random pure-composition particles from the measured data set
605 for each sample, mixing them virtually and determining, whether they would be detected as mixed.
606 This was carried out one time without any size restrictions and a second time with only selecting
607 particles not more than a factor of 3 different in size. The latter was done to account for the fact that
608 in a turbulent environment and in the regarded size range, the collision efficiency is highest for
609 particles of similar size (Pinsky et al. 1999; Wang et al. 2005).

610 **2.5.1 Simulating particle mixtures due to longer exposure times**

611 While in the modeling section particles are assumed to be spherical, this is typically not the case for
612 natural aerosol like mineral dust particles. Therefore, a second approach based on particles images
613 was used to estimate the effect of internal particle mixture on the substrate, i.e. taking into account



614 the real particle shapes. Due to the large number of images required, this approach could only be
615 used for assessing the size statistics, but not for the chemical composition. All segmented images of
616 each deposition sample were subject to particle size analysis. In following steps, a number of 2, 3, 5,
617 10, 15, or 20 segmented images of the same sample were combined into a single image, simulating
618 an extension of exposure time by the according factor. This approach inherently assumes a constant
619 size distribution during exposure and a random particle deposition. The resulting images were then
620 subject to the same particle analysis, yielding apparent size distributions after a coincidental mixing.
621 In contrast to the pure modeling approach, here the true size distribution is not known because even
622 the lowest coverage samples might contain internal mixtures. Certainly though, the lowest coverage
623 sample is closest to the true size distribution and therefore will be used as reference.

624 **3 Results and Discussion**

625 **3.1 Uncertainty of measurements for the new collection techniques and** 626 **determination of mixing state**

627 **3.1.1 Area homogeneity of collected particles**

628 ***Free-wing impactor (FWI)***

629 To assess the homogeneity of particle distribution, for each sample the center 80 mm² (about 65 % of
630 the total sample area) were scanned with approximately one thousand SEM images (approximately
631 one third coverage), and the average particle density was determined for each mm² as function of
632 d_g . For particles between 4 μm and 8 μm in diameter (see Fig. S4 in electronic supplement) no
633 systematic bias in particle density is visible, except for a slight enhancement toward the borders in a
634 few cases. The remaining variability remains probably linked to statistical uncertainty and surface
635 defects interpreted as particles by the automatic segmentation algorithm. However, the density
636 variations between each mm² remain below a factor of 2. As commonly 20 to 100 mm² are analyzed,
637 the inhomogeneity can be regarded as minor error. For larger particles, the uncertainty due to
638 counting statistics becomes dominant.

639 ***Dry particle deposition sampler (DPDS)***

640 Similar to above, for the DPDS deposition density homogeneity was assessed, but in this case nearly
641 all of the central 80 mm² were scanned. In about half of the samples, a crescent-shaped density
642 gradient can be observed (see Fig. S5 in electronic supplement). This gradient most probably
643 originates from a stationary wave introduced by the recession of the sample substrate slightly below
644 the primary plane of the DPDS. Depending on the analysis location, a bias in the range of factor 2 to 3
645 in deposited particle number can occur. Therefore, the fields of analysis for the chemical composition
646 and size distribution discussion below were homogeneously distributed over the sample surface at a
647 regular distance. Also with the DPDS, for larger particles the uncertainty due to counting statistics
648 becomes dominant.

649 **3.1.2 Impact of area coverage and counting statistics on size distribution and total** 650 **volume**

651 Fig. 6 shows the apparent number and volume size distributions of particles deposited from aerosols
652 with CV-ground or CV-air size distribution for different area coverages, equaling different exposure
653 times. As it is to be expected, for short exposure times there is a considerable counting error, which



654 decreases to less than 10 % for the smaller particles at area coverages of 0.01 and higher. In median,
655 no particle larger than 50 μm would be detected in deposition area for area coverages smaller than
656 0.0025, and more than 0.005 are necessary to collect more than 5 particles (not shown in graphs). As
657 opposing trend there is a bias in size distribution towards lower concentrations and larger particles,
658 which starts getting relevant at coverages of 0.1. This bias is introduced by the coincidental clumping,
659 a second particle depositing on an already deposited one. As result, for the given aerosol size
660 distributions, an area coverage of 0.03 to 0.05 seems most appropriate to get a size distribution
661 influenced least by counting errors and sampling/mixing bias.

662 Generally similar, but more pronounced effects can be observed, if the second approach – simulating
663 longer exposure times by combining real microscope images – is used. Fig. 7 shows for three samples
664 – low, medium and high area coverages – the evolution of the size distribution due to simulated
665 longer exposure times. In case of high dust deposition rates and long exposure times, particles
666 smaller than 10 μm in diameter would be underestimated by a factor of more than 2, while larger
667 particles would be considerable overrepresented. A shift in the modal diameter of 50 % towards
668 larger size could be the result. However, at the large end of the volume size distribution, counting
669 statistics might considerably influence the total particle mass uncertainty, even at these long
670 simulated exposition times.

671 If total mass deposition is estimated from the microscope images, one can set up a relation of total
672 volume and apparent area coverage, which might serve as a quick estimate of total deposited
673 particle mass (Fig. 8). If the result of the fit function is multiplied with an approximate particle
674 density, the result gives the deposition as mg/m^2 with an uncertainty of factor 2. As expected, the fit
675 function starts to underestimate the volume / mass for high area coverage.

676 When calculating total mass / volume from small amounts of material, special attention has to be
677 paid to the errors introduced by counting statistics. Table 1 gives an overview for deposition
678 simulation results based on a typical area, which would be used for automated single particle
679 analysis. Two size distributions were considered with different abundance of large particles. Using
680 the CV-ground size distribution, we observe an uncertainty of a factor of 2 for the total mass (95 %
681 two-sided confidence interval), when 3,000 particles are counted, which are equivalent to 8 μg of
682 mass. If only particles between 1 and 32 μm in diameter are regarded, a relative uncertainty of 20 %
683 is achieved with 1500 particles. When analyzing about 100 μg of particle mass, the statistical error is
684 in the range of 30 % mass in case of CV-ground size distribution and 15 % for CV-air. It can be
685 concluded here that a minimum number of 5,000 to 10,000 single particle measurements would be
686 desirable to stabilize the total mass concentration in the range of 10 % uncertainty. As this number is
687 usually not reached in SEM studies (e.g., Reid et al. 2003; Coz et al. 2009; Kandler et al. 2011a),
688 additional attention should be paid to larger particles, e.g. by analyzing larger sample areas, to
689 decrease the uncertainty in mass (see also Fig. 4). Note that the same considerations in principle
690 apply to bulk investigations, when only small amounts of mass are analyzed, but are not commonly
691 stated.

692 3.1.3 Amount of coincidental internal particle mixtures

693 When assessing the mixing state of particles from an offline single particle technique, coincidental
694 internal particle mixture has to be taken into account. Fig. 9 shows the upper 95 % confidence limit
695 of apparent fractions of internally mixed particles for a two-component system as function of source
696 component ratio and area coverage for detectable strong internal mixtures (refer to section 2.5; data



697 are given in the electronic supplement, Table S2 and Table S3). These numbers can be considered as
698 detection limit for fractions of internal mixed particles. As to be expected, higher area coverage
699 yields higher mixture probability. No significant mixture for submicron particles occurs in these cases.
700 In particular, if both components are present in equal amounts, mixing probabilities become high
701 already for covered area fraction of a few percent. Note also the different size maximum for strong
702 versus detectable mixture.

703 Applying the same model type based on the CV-ground size distribution to a ternary modal
704 composition distribution of sulfate, sea-salt and dust as described in section 2.5, mixing probabilities
705 for a specific atmospheric composition can be estimated (Fig. 10). Note the different color bar scale.
706 It becomes instantly obvious that the mixing probabilities are much lower than in the homogeneous
707 case. Mixtures between sulfate and sea-salt as well as ternary mixture are absent. The relative
708 fraction of internally mixed particles is lower by an order of magnitude. This can be explained by the
709 fact that the defined relative detection limits of 20 % and 1 % restrict the detection of mixing to
710 mixing partners not differing in size by more than a factor of 1.59 (strong mixing) and 4.6 (detectable
711 mixing). But because different aerosol type are mainly present in different size regimes here
712 (Schladitz et al. 2011), the mixture can only be efficient for size ranges, where these component have
713 an overlap. In general, however, also here mixture increases with particle size.

714 It can be concluded here that mixing studies for large particles are generally very difficult. Many
715 particles need to be collected in total to ensure reliable counting statistics, which leads in
716 consequence to high mixing probabilities. This issue is of less concern for particles smaller than 10
717 μm for the given size distributions and in cases, where the aerosol has a strong dependence of
718 composition on particle size. It also emphasizes that mixing studies should be accompanied by
719 mixture modeling as performed below.

720 **3.2 Field Measurements – methodical aspect**

721 **3.2.1 Comparison of atmospheric size and volume concentrations**

722 Using the FWI sampling efficiencies outlined in section 2.3.3 and the DPDS deposition velocities from
723 2.4.1, one can calculate the atmospheric size distribution derived by the two techniques. Fig. 11
724 shows the average size distributions for the post- and pre-storm periods based on different
725 deposition velocity models for total and upper estimate dust mass concentrations. The lower dust
726 estimate (not shown) exhibits qualitatively the same behavior. It is evident that there is a large
727 discrepancy between the different models as well as between the DPDS and FWI measurements. The
728 discrepancy is clearly larger than the statistical uncertainties. While the total mass median diameter
729 derived from DPDS (Piskunov model) is around 5 μm particle diameter, for the FWI it is
730 approximately 25 μm . A dust size distribution measured in the Saharan Air Layer in 2.3 km altitude
731 (computed from data shown by Weinzierl et al. 2017) contains the same mode around 4 μm
732 diameter, but shows a secondary maximum at 10 μm , which is not found by the ground-based
733 measurements. It is interesting to note that these values get closer, when only the dust fraction is
734 considered, indicating a connection of the discrepancy with the hygroscopic growth (e.g., growth or
735 density misestimate). Two other reasons for the discrepancy might be for the FWI an uncertain
736 collection efficiency and particle losses due to non-parallel flow for the DPDS. The FWI has 50 %
737 collection efficiency around 11 μm particle aerodynamic diameter, so for smaller particles – the
738 majority by far – the efficiency correction function may yield unrealistic values. The DPDS model
739 assumptions require a well oriented flow. At the high wind speeds, a non-zero angle-of-attack flow



740 (from below) might lead to considerable particle losses for the larger particles. This might for
741 example be caused by an increased boundary layer thickness over the lower plate. Such an angular
742 flow was observed at the measurement site due to the cape orography.

743 When total mass is calculated from deposition, it can be compared to dust concentration
744 measurements with a high volume filter sampler. Fig. 12 shows time series of mass concentrations
745 measured by the high-volume sampler, estimated from dry deposition measurements as well as the
746 raw dry deposition flux densities. For dry deposition uncertainties derived from the low / upper
747 estimates as well as from counting statistics are shown. A few things can be learned from this data.
748 With respect to the deposition model, the Piskunov model performs rather well. The average of the
749 high-volume sampler mass concentration time series (see Table 2) is close to the lower estimate of
750 the Piskunov model, while the higher estimate overestimates the mass concentration. The other
751 models deviate considerably more, as to be expected from the deposition velocity differences (Fig.
752 5). The ratio of the mass concentration estimate to the mass flux density varies over slightly more
753 than one order of magnitude, depending mainly on size distribution and wind conditions. High
754 volume and deposition-estimated mass concentrations as well as the mass flux densities follow
755 qualitatively the same pattern in showing low concentration and high concentration periods. The
756 absolute numbers, however, deviate significantly. For sub-periods, the correlation quality seems to
757 be different. E.g., starting from June 21, the correlation of mass flux with high volume mass
758 concentrations seems to be better than the one with deposition estimated concentrations; for the
759 period before June 21 situation is converse. No direct link of the correlations with any meteorological
760 variable was found, indicating that the deviations depend in part on erroneous assumptions in the
761 model. For example, tuning other deposition velocity models by arbitrary factors can lead to a better
762 agreement of actively and passively determined mass concentrations for this particular data set (Fig.
763 S9 in electronic supplement), but the data basis is too small for a robust tuning without physical
764 backing. Moreover, disagreement might also be caused by physical measurement biases like
765 unknown size-dependent inlet efficiency for the high-volume sampler or angular inflow for the DPDS.

766 3.3 Field Measurements – atmospheric and aerosol aspects

767 3.3.1 Aerosol composition

768 Overall aerosol composition (i.e. the relative number abundance of the different particle groups) was
769 measured by electron microscopy single particle analysis (Fig. 13). The relative abundance of soluble
770 sulfate is highest for the smallest particle sizes, which is in good accordance with previous
771 measurements in the eastern Atlantic Ocean (Kandler et al. 2011a). After the storm passage, higher
772 sulfate abundances – soluble as well as stable – are observed in 2013, which are similar to those
773 observed in 2016. The sea-salt abundance is higher for the pre-storm period in 2013, which is in
774 agreement with the wind speeds observed (see below). In 2016, a much higher abundance of small
775 Fe-rich particles (contained in the oxides/hydroxides class) is observed compared to the pre-storm
776 period in 2013. For the post-storm period in 2013, minor amounts of these particles are visible.

777 Overall, an average dust deposition of $10 \text{ mg m}^{-2} \text{ d}^{-1}$ (range $0.5\text{--}47 \text{ mg m}^{-2} \text{ d}^{-1}$) is observed (Fig. 14).
778 While a strict disambiguation can't be done elements also found in sea-salt, Al, Si, P, Ti, and Fe are
779 most like derived from dust only and are therefore also shown in the graph. At Barbados, Fe
780 contributes $0.67 (0.01\text{--}3.3) \text{ mg m}^{-2} \text{ d}^{-1}$ to deposition, while phosphorous adds only $0.001 \text{ mg m}^{-2} \text{ d}^{-1}$;
781 however, P is below the detection limit on two thirds of the days. The cumulative size distribution
782 shows that in particular P and Ti are located preferentially within smaller particles. Al, Si and Fe show



783 generally a similar size distribution. As corroborated by the results above, Fe is slightly more present
784 in particles smaller than 5 μm , but the impact of these periods with small Fe-rich particles on total Fe
785 deposition is obviously small, owing to the lower overall deposition rate during these periods.

786 3.3.2 Airmass history and potential aerosol sources

787 The airmass provenance of the sampling periods in 2013 and 2016 is generally similar. The
788 trajectories mostly followed the trade-wind path from North-West Africa and East Atlantic Ocean to
789 Barbados (Fig. S6 in electronic supplement). In 2013, the air was coming more frequently from
790 Western African than in 2016. After the tropical storm Chantal in 2013, the airmass origin shifted
791 slightly to more southern regions. In a few cases in 2013, air from the North-West Atlantic Ocean was
792 recirculated into the trade-wind path. In 2016, airmasses from North-East Southern America were
793 more frequent than in 2016.

794 The sea-salt deposition rates are not linked to air mass provenance (not shown). The dust
795 provenance for both years (Fig. 15) is – as expected – pointing to West Africa. This source region is
796 also identified by isotope measurements in July/August 2013 (Bozlaker et al. 2018). The soluble
797 sulfate deposition is generally linked to three regions, the Atlantic Ocean, West Africa and south west
798 Europe. In particular in 2016, the sulfate sources appear to be located more in Europe and less in
799 Africa. The relative ion balance shows mostly slightly negative values indicating presence of NH_4^+ or
800 H^+ . Interestingly, a positive ion excess is observed for European sulfate in 2016, indicating possible
801 presence of NO_3^- . These observations support the hypothesis that sulfate associated with dust events
802 at Barbados partly might originate from secondary processing of European precursors (Li-Jones et al.
803 1998).

804 Iron contribution from dust is of particular interest for marine ecosystems. Therefore, Fig. 16 shows
805 in the upper panel the silicate SIAI as proxy for quick iron availability. It is obvious, that the iron-
806 containing silicate particle source is located in West Africa. Northern and southern West Africa as
807 source regions can't be distinguished after trans-Atlantic transport, in contrast to investigations close
808 to the source (Kandler et al. 2007). This is consistent with observations based on isotope analysis,
809 where also a homogeneous composition has been observed at Barbados (Bozlaker et al. 2018). In
810 comparison with Fig. 15, a slightly higher SIAI can be observed in 2016 than in 2013, while the dust
811 deposition rates in contrast are lower. While the total iron deposition correlates well with dust
812 deposition (not shown), similar to observations by Trapp et al. (2010), for the SIAI an inverse
813 relationship is found at Barbados with higher dust deposition rates leading to lower ratios of SIAI to
814 total dust. This correlates to previous findings, where iron solubility decreased with increasing dust
815 concentration (Shi et al. 2011b; Sholkovitz et al. 2012), though no direct causal relationship can be
816 derived (Shi et al. 2011a). As the finding indicates a higher iron contribution from smaller particles,
817 the lower row of Fig. 16 shows the Fe contribution by small iron-rich grains. While in 2013 the
818 contribution of this particle type is generally low, in 2016, when trajectories cross the North-Eastern
819 tip of South America, there is a low input during low-dust situations. However, trajectories arriving
820 straight from south east would also cross Barbados before arrival, so there might also local
821 contribution from the island. Taking a closer look at these particles (Fig. S7 in the electronic
822 supplement) it reveals that they differ in structure from usual mineral dust particles (Moreno et al.
823 2006; Scheuven et al. 2011; Deboudt et al. 2012), but resemble more closely material from
824 industrial or combustion processes (Fu et al. 2014; Hu et al. 2015; Li et al. 2016). This observation is
825 interpreted as evidence for an anthropogenic iron input into a marine environment. This is of



826 particular interest, as according to previous work, the bioavailability of anthropogenic iron is usually
827 higher than provided by natural sources (Desboeufs et al. 2005; Sedwick et al. 2007; Fu et al. 2014).

828 3.3.3 Sea-salt composition

829 When considering sea-salt composition, it is assumed generally that except from the sulfate content,
830 aerosol produced from sea-water has a major composition resembling the bulk sea-water (Lewis et
831 al. 2004). However, it was recently shown in the Arctic that a fractionation can occur also with
832 respect to the major composition (Salter et al. 2016). At Barbados, an increasing positive deviation
833 from the nominal value of 0.022 with decreasing particle size is observed for the Ca/Na atomic ratio
834 of sea-salt particles (Fig. 17). This indicates that the same effects found by Salter et al. (2016) are
835 present in Caribbean sea-salt production. According to the authors, these might be linked to an
836 enrichment of Ca in sea surface micro-layers, but details are not yet known.

837 3.3.4 Abundance of mixed particles

838 If we consider the abundance of mixed particles at Barbados, a complex picture emerges as function
839 of particle size, time period and available mixing partners (Fig. 18). It can be observed that the total
840 deposition rate for all particle types is linked to the wind speed, what is to be expected from the
841 physical process (see for example Fig. S8 in electronic supplement). The higher sea-salt deposition
842 rates and also higher concentrations in 2013 in comparison to 2016 are also linked to the wind
843 speed, showing the local sea-salt production. In contrast, the dust concentration is slightly lower for
844 higher wind speeds (Fig. S8) for both years. With increasing particle size, the relative abundance of
845 internal dust/sea-salt mixtures increases (Fig. 18), but these mixtures only occur when considerable
846 amounts of sea-salt are present. This is different for the internal mixture with sulfate. While there
847 are similar ratios of dust and sulfate particles observed in the second half of the 2013 data as in
848 2016, in 2013, dust/sulfate mixtures are practically absent. Assuming that higher wind speeds in 2013
849 should lead to more internal mixing due to increased turbulence, this is clearly indicating that in
850 contrast to the sea-salt/dust mixture, the sulfate/dust mixture has a non-local origin (e.g., Usher et
851 al. 2002).

852 This is corroborated by the dependence of internal mixtures relative abundance on the single mixing
853 probability (Fig. S10 in the electronic supplement). If one considers here the binary number fraction
854 of mixed particles – i.e. ratio of binary mixed particles to pure compounds – as function of the size-
855 restricted single mixing probability, there is a weak positive correlation for dust/sea-salt mixtures for
856 particles larger than 2 μm diameter, but no correlation for dust/sulfate mixtures. Moreover, for
857 similar single mixing probabilities, the binary number fraction of mixed particles appears slightly
858 higher for higher deposition rates. As the collision efficiency depends on the square of the number
859 concentration (Sundaram et al. 1997), this supports the hypothesis of a locally produced internal
860 mixture of sea-salt and dust and a non-local production of sulfate and dust, the latter having most
861 probably cloud processing involved (Andreae et al. 1986; Niimura et al. 1998).

862 The overall ratio of dust/sea-salt internal mixture abundance to all dust- and sea-salt-particles
863 increases from 0.01–0.03 for 1 μm particles to 0.1–0.7 for particles of 8–16 μm in diameter, whereas
864 for dust/sulfate mixtures the ratio of 0.01–0.02 is not dependent on particle size. Denjean et al.
865 (2015) report mixed particle abundances of 0.16–0.3, but do not state a size range, so the data can't
866 be compared directly.



867 If the findings on Barbados are compared to measurements in the eastern Atlantic Ocean (Kandler et
868 al. 2011a), a generally lower abundance of internally mixed particles with respect to dust/sulfate is
869 observed, while comparable abundances of sea-salt/dust mixtures are found. While the latter can be
870 explained by similar wind conditions and comparable single mixing probabilities, the former seems to
871 be caused by different aging conditions. Dust arriving over Barbados is transported mostly in the dry
872 Saharan Air Layer (e.g., Schütz 1980), while dust arriving during winter-time at Cape Verde is
873 transported inside the humid marine boundary layer (Chiapello et al. 1995; Kandler et al. 2011b).
874 Therefore, considerably higher chemical processing rates at Cape Verde due to the higher humidity
875 can be expected (Dlugi et al. 1981; Ullerstam et al. 2002), even though the transport time is most
876 likely shorter. In addition, the boundary layer most probably provides higher concentrations of sulfur
877 compounds for reaction (Davison et al. 1996; Andreae et al. 2000).

878 ***Change in dust behavior due to internal particle mixing***

879 If dust particles become internally mixed, their mass, size and hygroscopic behavior change.
880 Therefore, they will have modified deposition velocities as well as hygroscopic properties. Fig. 19
881 shows the increases in deposition velocities for mixed particles observed at Ragged Point in 2013 and
882 2016. For the both mixtures (dust/sea-salt and dust/sulfate), an increase at ambient conditions of a
883 factor of 2–3 is observed for submicron dust particles, which rises to a factor of 5–10 for particles of
884 3 μm dust core diameter. As a result, the dust average deposition velocity for particles between 1
885 and 10 μm aerodynamic diameter is increased by 30–140 % at ambient conditions (Fig. 20).
886 Considering a mass mean aerodynamic diameter in deposition of 7.0 μm , at ambient conditions dust
887 deposition velocity is 6.4 mm/s, which is an enhancement by approximately 35 % over the unmixed
888 state. This overall value is in the range estimated by Prospero et al. (2009). The enhancement will
889 become more pronounced at higher humidities. It has to be emphasized that this estimate is a lower
890 limit, as there most likely exist mixed particles with a smaller contribution of hygroscopic material,
891 which remaining undetected by our analytical approach. At higher humidities, this smaller
892 contribution nevertheless will increase the deposition velocity of the mixtures. While we observe
893 similar relative abundances of mixed particles to previous work in Asian dust outflow Zhang (2008),
894 our estimate of impact on deposition is considerable higher, which is mainly related to the use of the
895 Piskunov model taking into account turbulent deposition over a Stokes settling approach.

896 An internal mixture of dust with a soluble compound will also modify the in-cloud behavior of the
897 dust particles. As Denjean et al. (2015) have shown, in the Caribbean only dust particles internally
898 mixed with soluble compounds exhibit considerable hygroscopic growth. Therefore, if the mixed dust
899 particles are entrained into a cloud, they would preferentially be activated into a cloud droplet in
900 comparison to unmixed dust. This according cloud droplets would then contain a potential effective
901 ice-nucleating particle (DeMott et al. 2003). Because the ice-nucleating efficiency of a mixed droplet
902 would follow the most efficient compound (Augustin-Bauditz et al. 2016), these droplets would at
903 according temperatures become ice particles by immersion freezing (Marcolli et al. 2007; Niemand et
904 al. 2012). We may hypothesize that along this path – by internal mixture with soluble compounds –
905 the atmospheric ice-nucleating efficiency of dust particles could be enhanced. For example, within
906 mixed-phase clouds at a free-troposphere station, high abundances of internally mixed particles
907 were found as ice-nucleating particles or ice particle residues (Ebert et al. 2011; Worringen et al.
908 2015). Note that this mixing path is probably restricted to immersion freezing (Eastwood et al. 2009).



909 **4 Summary and Conclusions**

910 Aerosol deposition measurements by means of passive samplers were carried out on a daily basis at
911 Ragged Point, Barbados in June/July 2013 and August 2016. In addition, active aerosol collection was
912 performed with a cascade and a novel free-wing impactor. Size, shape and composition of about
913 110,000 particles were determined by electron microscopy. Focus was placed in this work on
914 measurement accuracy of chemical composition and mixing state determination for individual
915 particles.

916 Ragged Point, in particular in 2013, is a high-wind and high-humidity environment, which
917 considerably influences representativeness and accuracy of the different sampling techniques. A
918 deposition model including chemistry-dependent hygroscopic growth was adapted to the sampling
919 situation to assess atmospheric concentration of large particles. Fair agreement was reached
920 between passive and active techniques regarding mass concentration, but clear discrepancies were
921 observed for particle size distribution.

922 Special attention was paid to the mixing state of dust particles. A model was developed to assess the
923 mixing state of airborne particles by correcting for sampling artifacts due to particle overload leading
924 to coincidental internal mixing of particles on the substrate (i.e., not representative for the airborne
925 state). Different approaches were tested based on model size distributions and observed particle
926 deposition images. It was found that the size distribution is only weakly affected for substrate area
927 coverages with particles below 10 %. The chemical composition of mixtures, however, is already
928 affected at much lower area coverages of < 1 %.

929 During our measurement campaigns, the aerosol was dominated by dust, sea-salt and sulfate in
930 changing proportions. The sea-salt concentration at Ragged Point is mainly depending on wind
931 speed. Back trajectory analysis showed that dust is originating from the usual sources in West Africa.
932 Sulfate showed three major potential source areas, Africa, Europe and Atlantic Ocean. Particularly in
933 2013, sulfate was more linked to the African source, while in 2016 southwest Europe occurred as
934 potential source, with a possible contribution of nitrate. In 2016 for short time periods, contributions
935 to iron deposition from probably anthropogenic sources (potentially as magnetite) from South
936 America or the island of Barbados were observed.

937 It was further found that internal mixing of dust and sea-salt is depending on local wind speed, and
938 we, thus, hypothesize that it is produced locally, most likely by turbulent processes. In contrast,
939 mixtures of dust and soluble sulfates are presumably not produced locally, but may have formed
940 during the inter-continental transport. Even though the overall amount of internally mixed particles
941 is comparatively low, a considerable impact on total dust deposition velocity is estimated. In
942 addition, a pathway is hypothesized by which the ice-nucleation efficiency of dust can be increased
943 by mixing with soluble compounds during or after the long-range transport.

944 For future work, some conclusions can be drawn from our observations:

- 945 • If different techniques for deposition and/or atmospheric concentration measurements are
946 compared, it is crucial to measure particles size distributions. We observed in some cases
947 that total mass concentration can compare rather well, even though size distributions – and
948 therefore collection efficiencies – are considerably different.



- 949
- 950
- 951
- 952
- 953
- 954
- 955
- 956
- 957
- 958
- 959
- 960
- 961
- 962
- 963
- 964
- 965
- 966
- 967
- 968
- 969
- 970
- A better understanding – in theory as well as in experimental use – of particle deposition and collection efficiencies is required in particular under high wind-situations, where turbulent transport has a considerable impact. This most probably applies to a wide range of deposition samplers, not only these used in this work.
 - When mixing state investigations are done based on collected aerosol particles, the impact of coincidental mixtures on the substrate must be assessed, unless the area coverage with particles is very low ($\ll 1\%$). This is particularly the case for larger particles ($> 5 \mu\text{m}$ diameter) and for aerosols in the same size range, where similar abundances of different mixing partners exist.
 - Internal particle mixing most likely has a considerable influence on dust deposition speed and on the impact of dust on clouds. Future models regarding dust deposition should take a deposition speed enhancement by internal mixing into account. However, more systematic investigations are needed to better understand the mixing processes.
 - With respect to the cloud impact if mixing via a more efficient incorporation of immersion freezing ice nuclei into cloud droplets by preferential activation, future ice nucleation chamber experiments are needed to assess the importance of this effect.
 - Finally, a larger data basis beyond the observation of single events is required to assess the anthropogenic influence on the iron deposition into the Oceans, besides the input by mineral dust. This data base needs to be acquired with a high time resolution (maximum days) to match the duration of the observed deposition events. Also, these time series would need to cover months to years at Barbados, given the probably infrequent occurrence of these events.

971 **5 Data availability**

972 The data sets of all particles used for this investigation including particle size, shape, and composition
973 are given as text tables in the electronic supplement along with a data overview.

974 **6 Author contribution**

975 KK designed the experiment. KK and MH carried out field work in 2013. MP and CP carried out the
976 field work in 2016. KK and KS analyzed the samples. KK programmed the models and data processing
977 code. KK, SW and ME analyzed data and prepared the manuscript. All authors contributed in data
978 discussion and manuscript finalization.

979 **7 Competing interests**

980 The authors declare that they have no conflict of interest.

981 **8 Acknowledgements**

982 We acknowledge financial support from the German Research foundation (DFG grant KA 2280/2-1
983 and KA 2280/3-1). We thank Joseph Prospero for his valuable comments on the manuscript and
984 discussion; his wind and mass concentration data were obtained under National Science Foundation
985 (NSF) grant AGS-0962256. The authors gratefully acknowledge the NOAA Air Resources Laboratory



986 (ARL) for the provision of the HYSPLIT transport and dispersion model and/or READY website
987 (<http://www.ready.noaa.gov>) used in this publication.

988 **9 Literature**

- 989 Agresti, A., B. A. Coull (1998): Approximate Is Better than "Exact" for Interval Estimation of Binomial
990 Proportions. *Am. Stat.* 52(2), 119-126. doi: 10.2307/2685469
- 991 Aluko, O., K. E. Noll (2006): Deposition and Suspension of Large, Airborne Particles. *Aerosol Sci.*
992 *Technol.* 40(7), 503-513.
- 993 Andreae, M. O. (1995). Climatic effects of changing atmospheric aerosol levels. Future climates of the
994 world: a modelling perspective. A. Henderson-Sellers. Amsterdam, The Netherlands, Elsevier.
995 **16:** 347-398.
- 996 Andreae, M. O., R. J. Charlson, F. Bruynseels, H. Storms, R. V. Grieken, W. Maenhaut (1986): Internal
997 Mixture of Sea Salt, Silicates, and Excess Sulfate in Marine Aerosols. *Science* 232, 1620-1623.
- 998 Andreae, M. O., W. Elbert, R. Gabriel, D. W. Johnson, S. Osborne, R. Wood (2000): Soluble ion
999 chemistry of the atmospheric aerosol and SO₂ concentrations over the eastern North
1000 Atlantic during ACE-2. *Tellus B* 52(4), 1066-1087. doi: 10.3402/tellusb.v52i4.17087
- 1001 Armstrong, J. T. (1991). Quantitative elemental analysis of individual microparticles with electron
1002 beam instruments. Electron probe quantitation. K. F. J. Heinrich and D. E. Newbury. New
1003 York, Plenum Press: 261-315.
- 1004 Ashbaugh, L. L., W. C. Malm, W. Z. Sadeh (1985): A residence time probability analysis of sulfur
1005 concentrations at grand Canyon National Park. *Atmos. Environ.* 19(8), 1263-1270. doi:
1006 10.1016/0004-6981(85)90256-2
- 1007 Augustin-Bauditz, S., H. Wex, C. Denjean, S. Hartmann, J. Schneider, S. Schmidt, M. Ebert, F.
1008 Stratmann (2016): Laboratory-generated mixtures of mineral dust particles with biological
1009 substances: characterization of the particle mixing state and immersion freezing behavior.
1010 *Atmos. Chem. Phys.* 16(9), 5531-5543. doi: 10.5194/acp-16-5531-2016
- 1011 Baker, A. R., T. D. Jickells (2006): Mineral particle size as a control on aerosol iron solubility.
1012 *Geophysical Research Letters* 33(17), L17608. doi: 10.1029/2006gl026557
- 1013 Bozlaker, A., J. M. Prospero, J. Price, S. Chellam (2018): Linking Barbados Mineral Dust Aerosols to
1014 North African Sources Using Elemental Composition and Radiogenic Sr, Nd, and Pb Isotope
1015 Signatures. *J. Geophys. Res.* 123(2), 1384-1400. doi: doi:10.1002/2017JD027505
- 1016 Carpenter, J., J. Bithell (2000): Bootstrap confidence intervals: when, which, what? A practical guide
1017 for medical statisticians. *Stat. Med.* 19(9), 1141-1164. doi: 10.1002/(sici)1097-
1018 0258(20000515)19:9<1141::aid-sim479>3.0.co;2-f
- 1019 Chiapello, I., G. Bergametti, L. Gomes, B. Chatenet, F. Dulac, J. Pimenta, E. Santos Soares (1995): An
1020 additional low layer transport of Sahelian and Saharan dust over the North-Eastern Tropical
1021 Atlantic. *Geophys. Res. Lett.* 22(23), 3191-3194. doi: 10.1029/95GL03313
- 1022 Choobari, O. A., P. Zawar-Reza, A. Sturman (2014): The global distribution of mineral dust and its
1023 impacts on the climate system: A review. *Atmos. Res.* 138(0), 152-165. doi:
1024 10.1016/j.atmosres.2013.11.007
- 1025 Cliff, G., G. W. Lorimer (1975): The quantitative analysis of thin specimens. *J. Microsc.* 103(2), 203-
1026 207. doi: 10.1111/j.1365-2818.1975.tb03895.x
- 1027 Coz, E., F. J. Gómez-Moreno, M. Pujadas, G. S. Casuccio, T. L. Lersch, B. Artífano (2009): Individual
1028 particle characteristics of North African dust under different long-range transport scenarios.
1029 *Atmos. Environ.* 43, 1850-1863.
- 1030 Dall'Osto, M., R. M. Harrison, E. J. Highwood, C. O'Dowd, D. Ceburnis, X. Querol, E. P. Achterberg
1031 (2010): Variation of the mixing state of Saharan dust particles with atmospheric transport.
1032 *Atmos. Environ.* 44(26), 3135-3146. doi: 10.1016/j.atmosenv.2010.05.030
- 1033 Davison, B., C. O'Dowd, C. N. Hewitt, M. H. Smith, R. M. Harrison, D. A. Peel, E. Wolf, R. Mulvaney, M.
1034 Schwikowski, U. Baltensperger (1996): Dimethyl sulfide and its oxidation products in the



- 1035 atmosphere of the Atlantic and Southern Oceans. *Atmos. Environ.* 30(10), 1895-1906. doi:
1036 10.1016/1352-2310(95)00428-9
- 1037 Deboudt, K., P. Flament, M. Choël, A. Gloter, S. Sobanska, C. Colliex (2010): Mixing state of aerosols
1038 and direct observation of carbonaceous and marine coatings on African dust by individual
1039 particle analysis. *J. Geophys. Res.* 115, D24207. doi: 10.1029/2010JD013921
- 1040 Deboudt, K., A. Gloter, A. Mussi, P. Flament (2012): Red-ox speciation and mixing state of iron in
1041 individual African dust particles. *J. Geophys. Res.* 117, D12307. doi: 10.1029/2011JD017298
- 1042 Deer, W. A., R. A. Howie, J. Zussman (1992): *An Introduction to the Rock-Forming Minerals*. Second
1043 Edition. Harlow, UK, Pearson Education Ltd.
- 1044 DeMott, P., K. Sassen, M. Poellot, D. Baumgardner, D. Rogers, S. Brooks, A. Prenni, S. Kreidenweis
1045 (2003): African dust aerosols as atmospheric ice nuclei. *Geophys. Res. Lett.* 30, 1732. doi:
1046 10.1029/2003GL017410
- 1047 Denjean, C., S. Caquineau, K. Desboeufs, B. Laurent, M. Maille, M. Quiñones Rosado, P. Vallejo, O. L.
1048 Mayol-Bracero, P. Formenti (2015): Long-range transport across the Atlantic in summertime
1049 does not enhance the hygroscopicity of African mineral dust. *Geophys. Res. Lett.* 42(18),
1050 7835-7843. doi: 10.1002/2015gl065693
- 1051 Desboeufs, K. V., A. Sofikitis, R. Losno, J. L. Colin, P. Ausset (2005): Dissolution and solubility of trace
1052 metals from natural and anthropogenic aerosol particulate matter. *Chemosphere* 58(2), 195-
1053 203. doi: 10.1016/j.chemosphere.2004.02.025
- 1054 DiCiccio, T. J., B. Efron (1996): Bootstrap confidence intervals. *Statist. Sci.* 11(3), 189-228. doi:
1055 10.1214/ss/1032280214
- 1056 Dlugi, R., S. Jordan, E. Lindemann (1981): The heterogeneous formation of sulfate aerosols in the
1057 atmosphere. *J. Aerosol Sci.* 12(3), 185-197. doi: 10.1016/0021-8502(81)90089-6
- 1058 Eastwood, M. L., S. Cremel, M. Wheeler, B. J. Murray, E. Girard, A. K. Bertram (2009): Effects of
1059 sulfuric acid and ammonium sulfate coatings on the ice nucleation properties of kaolinite
1060 particles. *Geophys. Res. Lett.* 36, L02811.
- 1061 Ebert, M., A. Worringer, N. Benker, S. Mertes, E. Weingartner, S. Weinbruch (2011): Chemical
1062 composition and mixing-state of ice residuals sampled within mixed phase clouds. *Atmos.*
1063 *Chem. Phys.* 11, 2805-2816. doi: 10.5194/acp-11-2805-2011
- 1064 Efron, B. (1979): Bootstrap Methods: Another Look at the Jackknife. *Ann. Statist.*(1), 1-26. doi:
1065 10.1214/aos/1176344552
- 1066 Efron, B. (2003): Second Thoughts on the Bootstrap. *Statist. Sci.* 18(2), 135-140. doi:
1067 10.1214/ss/1063994968
- 1068 Eglinton, T. I., G. Eglinton, L. Dupont, E. R. Sholkovitz, D. Montluçon, C. M. Reddy (2002):
1069 Composition, age, and provenance of organic matter in NW African dust over the Atlantic
1070 Ocean. *Geochem. Geophys. Geosy.* 3(8), 1-27. doi: 10.1029/2001gc000269
- 1071 Falkovich, A. H., E. Ganor, Z. Levin, P. Formenti, Y. Rudich (2001): Chemical and mineralogical analysis
1072 of individual mineral dust particles. *J. Geophys. Res.* 106(D16), 18029-18036.
- 1073 Fitzgerald, E., A. P. Ault, M. D. Zauscher, O. L. Mayol-Bracero, K. A. Prather (2015): Comparison of the
1074 mixing state of long-range transported Asian and African mineral dust. *Atmos. Environ.* 115,
1075 19-25. doi: 10.1016/j.atmosenv.2015.04.031
- 1076 Fletcher, R. A., N. W. M. Ritchie, I. M. Anderson, J. A. Small (2011). *Microscopy and microanalysis of*
1077 *individual collected particles. Aerosol Measurement. Principles, Techniques, and*
1078 *Applications*. P. Kulkarni, P. A. Baron and K. Willeke. Hoboken, New Jersey, John Wiley &
1079 Sons.: 179-232.
- 1080 Fu, H. B., G. F. Shang, J. Lin, Y. J. Hu, Q. Q. Hu, L. Guo, Y. C. Zhang, J. M. Chen (2014): Fractional iron
1081 solubility of aerosol particles enhanced by biomass burning and ship emission in Shanghai,
1082 East China. *Sci. Total Environ.* 481, 377-391. doi: 10.1016/j.scitotenv.2014.01.118
- 1083 Goldstein, J. I., D. E. Newbury, D. Joy, C. Lyman, P. Echlin, E. Lifshin, L. Sawyer, J. Michael (2003):
1084 *Scanning Electron Microscopy and X-Ray Microanalysis*. New York, Kluwer Academic /
1085 Plenum Publishers.



- 1086 Golovin, M. N., A. A. Putnam (1962): Inertial impaction on single elements. *Ind. Eng. Chem. Fundam.*
1087 1(4), 264-273.
- 1088 Grini, A., G. Myhre, C. S. Zender, I. S. A. Isaksen (2005): Model simulations of dust sources and
1089 transport in the global atmosphere: Effects of soil erodibility and wind speed variability. *J.*
1090 *Geophys. Res.* 110, 10.1029/2004JD005037.
- 1091 Hangal, S., K. Willeke (1990): Overall efficiency of tubular inlets sampling at 0 - 90 degrees from
1092 horizontal aerosol flows. *Atmos. Environ.* 24A, 2379-2386. doi: 10.1016/0960-
1093 1686(90)90330-P
- 1094 Hartung, J., B. Elpelt, K.-H. Klösener (2005): *Statistik: Lehr- und Handbuch der angewandten Statistik*,
1095 Oldenbourg, Munich, Germany.
- 1096 Hinds, W. C. (1999): *Aerosol Technology. Properties, behavior, and measurement of airborne*
1097 *particles*. Second edition. New York, USA, Wiley Interscience.
- 1098 Hu, Y., J. Lin, S. Zhang, L. Kong, H. Fu, J. Chen (2015): Identification of the typical metal particles
1099 among haze, fog, and clear episodes in the Beijing atmosphere. *Sci. Total Environ.* 511, 369-
1100 380. doi: 10.1016/j.scitotenv.2014.12.071
- 1101 Jaenicke, R., C. Junge (1967): Studien zur oberen Grenzgröße des natürlichen Aerosols. *Beitr. Phys.*
1102 *Atmos. / Contrib. Atmos. Phys.* 40, 129-143.
- 1103 Kandler, K., N. Benker, U. Bundke, E. Cuevas, M. Ebert, P. Knippertz, S. Rodríguez, L. Schütz, S.
1104 Weinbruch (2007): Chemical composition and complex refractive index of Saharan Mineral
1105 Dust at Izaña, Tenerife (Spain) derived by electron microscopy. *Atmos. Environ.* 41(37), 8058-
1106 8074. doi: 10.1016/j.atmosenv.2007.06.047
- 1107 Kandler, K., K. Lieke, N. Benker, C. Emmel, M. Küpper, D. Müller-Ebert, M. Ebert, D. Scheuvsens, A.
1108 Schladitz, L. Schütz, S. Weinbruch (2011a): Electron microscopy of particles collected at Praia,
1109 Cape Verde, during the Saharan Mineral dust experiment: particle chemistry, shape, mixing
1110 state and complex refractive index. *Tellus* 63B, 475-496. doi: 10.1111/j.1600-
1111 0889.2011.00550.x
- 1112 Kandler, K., L. Schütz, C. Deutscher, H. Hofmann, S. Jäckel, P. Knippertz, K. Lieke, A. Massling, A.
1113 Schladitz, B. Weinzierl, S. Zorn, M. Ebert, R. Jaenicke, A. Petzold, S. Weinbruch (2009): Size
1114 distribution, mass concentration, chemical and mineralogical composition, and derived
1115 optical parameters of the boundary layer aerosol at Tinfou, Morocco, during SAMUM 2006.
1116 *Tellus* 61B, 32-50. doi: 10.1111/j.1600-0889.2008.00385.x
- 1117 Kandler, K., L. Schütz, S. Jäckel, K. Lieke, C. Emmel, D. Müller-Ebert, M. Ebert, D. Scheuvsens, A.
1118 Schladitz, B. Šegvić, A. Wiedensohler, S. Weinbruch (2011b): Ground-based off-line aerosol
1119 measurements at Praia, Cape Verde, during the Saharan Mineral Dust Experiment:
1120 Microphysical properties and mineralogy. *Tellus* 63B, 459-474. doi: 10.1111/j.1600-
1121 0889.2011.00546.x
- 1122 Karyampudi, V. M., S. P. Palm, J. A. Reagen, H. Fang, W. B. Grant, R. M. Hoff, C. Moulin, H. F. Pierce,
1123 O. Torres, E. Browell, S. H. Melfi (1999): Validation of the Saharan Dust Plume Conceptual
1124 Model Using Lidar, Meteosat, and ECMWF Data. *Bull. Am. Met. Soc.* 80(6), 1045-1075.
- 1125 Karydis, V. A., A. P. Tsimpidi, S. Bacer, A. Pozzer, A. Nenes, J. Lelieveld (2017): Global impact of
1126 mineral dust on cloud droplet number concentration. *Atmos. Chem. Phys.* 17(9), 5601-5621.
1127 doi: 10.5194/acp-17-5601-2017
- 1128 Koehler, K. A., P. J. DeMott, S. M. Kreidenweis, O. B. Popovicheva, M. D. Petters, C. M. Carrico, E. D.
1129 Kireeva, T. D. Khokhlova, N. K. Shonija (2009): Cloud condensation nuclei and ice nucleation
1130 activity of hydrophobic and hydrophilic soot particles. *Phys. Chem. Chem. Phys.* 11, 7906-
1131 7920. doi: 10.1039/b905334b
- 1132 Kristensen, T. B., T. Müller, K. Kandler, N. Benker, M. Hartmann, J. M. Prospero, A. Wiedensohler, F.
1133 Stratmann (2016): Properties of cloud condensation nuclei (CCN) in the trade wind marine
1134 boundary layer of the western North Atlantic. *Atmos. Chem. Phys.* 16(4), 2675-2688. doi:
1135 10.5194/acp-16-2675-2016



- 1136 Lai, A. C. K., W. W. Nazaroff (2005): Supermicron particle deposition from turbulent chamber flow
1137 onto smooth and rough vertical surfaces. *Atmos. Environ.* 39(27), 4893-4900. doi:
1138 10.1016/j.atmosenv.2005.04.036
- 1139 Laskin, A., J. P. Cowin, M. J. Iedema (2006): Analysis of individual environmental particles using
1140 modern methods of electron microscopy and X-ray microanalysis. *J. Electron. Spectrosc.*
1141 *Relat. Phenom.* 150, 260-274. doi: 10.1016/j.elspec.2005.06.008
- 1142 Lepple, F. K., C. J. Brine (1976): Organic constituents in eolian dust and surface sediments from
1143 northwest Africa. *J. Geophys. Res.* 81(6), 1141-1147. doi: 10.1029/JC081i006p01141
- 1144 Lewis, E. R., S. E. Schwartz (2004): *Sea Salt Aerosol Production: Mechanisms, Methods,*
1145 *Measurements and Models.* Washington, DC, American Geophysical Union.
- 1146 Li-Jones, X., J. M. Prospero (1998): Variations in the size distribution of non-sea-salt sulfate aerosol in
1147 the marine boundary layer at Barbados: Impact of African dust. *J. Geophys. Res.* 103(D13),
1148 16073-16084. doi: 10.1029/98jd00883
- 1149 Li, S.-N., D. A. Lundgren (2002): Aerosol Aspiration Efficiency of Blunt and Thin-Walled Samplers at
1150 Different Wind Orientations. *Aerosol Sci. Tech.* 36, 342-350.
- 1151 Li, W., L. Shao, D. Zhang, C.-U. Ro, M. Hu, X. Bi, H. Geng, A. Matsuki, H. Niu, J. Chen (2016): A review
1152 of single aerosol particle studies in the atmosphere of East Asia: morphology, mixing state,
1153 source, and heterogeneous reactions. *J. Clean. Prod.* 112, 1330-1349. doi:
1154 10.1016/j.jclepro.2015.04.050
- 1155 Liao, H., J. H. Seinfeld (1998): Radiative forcing by mineral dust aerosols: sensitivity to key variables. *J.*
1156 *Geophys. Res.* 103(D24), 31637-31645. doi: 10.1029/1998JD200036
- 1157 Liu, B. Y. H., J. K. Agarwal (1974): Experimental observation of aerosol deposition in turbulent flow. *J.*
1158 *Aerosol Sci.* 5(2), 145-155. doi: 10.1016/0021-8502(74)90046-9
- 1159 Mahowald, N., S. Albania, J. F. Kok, S. Engelstaeder, R. Scanza, D. S. Ward, M. G. Flanner (2014): The
1160 size distribution of desert dust aerosols and its impact on the Earth system. *Aeolian Res.* 15,
1161 53-71. doi: 10.1016/j.aeolia.2013.09.002
- 1162 Marcolli, C., S. Gedamke, T. Peter, B. Zobrist (2007): Efficiency of immersion mode ice nucleation on
1163 surrogates of mineral dust. *Atmos. Chem. Phys.* 7, 5081-5091. doi: 10.5194/acp-7-5081-2007
- 1164 Matsuki, A., Y. Iwasaka, G.-Y. Shi, H.-B. Chen, K. Osada, D. Zhang, M. Kido, Y. Inomata, Y.-S. Kim, D.
1165 Trochine (2005): Heterogeneous sulfate formation on dust surface and its dependence on
1166 mineralogy: balloon-borne observations from balloon-borne measurements in the surface
1167 atmosphere of Beijing, China. *Water Air Soil Pollut.* 5(3), 101-132. doi: 10.1007/s11267-005-
1168 0730-3
- 1169 May, K. R., R. Clifford (1967): The impaction of aerosol particles on cylinders, spheres, ribbons and
1170 discs. *Ann. Occup. Hyg.* 10, 83-95.
- 1171 McInnes, L. M., D. S. Covert, P. K. Quinn, M. S. Germani (1994): Measurements of chloride depletion
1172 and sulfur enrichment in individual sea-salt particles collected from the remote marine
1173 boundary layer. *J. Geophys. Res.* 99(D4), 8257-8268. doi: 10.1029/93jd03453
- 1174 Moreno, T., X. Querol, S. Castillo, A. Alastuey, E. Cuevas, L. Herrmann, M. Mounkaila, J. Elvira, W.
1175 Gibbons (2006): Geochemical variations in aeolian mineral particles from the Sahara-Sahel
1176 Dust Corridor. *Chemosphere* 65, 261-270. doi: 10.1016/j.chemosphere.2006.02.052
- 1177 Munson, B. R., T. H. Okiishi, W. W. Huebsch, A. P. Rothmayer (2013): *Fundamentals of Fluid*
1178 *Mechanics*, 7th Edition, John Wiley & Sons.
- 1179 Niemand, M., O. Möhler, B. Vogel, H. Vogel, C. Hoose, P. Connolly, H. Klein, H. Bingemer, P. DeMott,
1180 J. Skrotzki, T. Leisner (2012): A Particle-Surface-Area-Based Parameterization of Immersion
1181 Freezing on Desert Dust Particles. *J. Atmos. Sci.* 69(10), 3077-3092. doi: 10.1175/jas-d-11-
1182 0249.1
- 1183 Niimura, N., K. Okada, X.-B. Fan, K. Kai, K. Arao, G.-Y. Shi, S. Takahashi (1998): Formation of Asian
1184 Dust-Storm Particles Mixed Internally with Sea Salt in the Atmosphere. *J. Meteor. Soc. Japan*
1185 76(2), 275-288.
- 1186 NOAA-ARL. (2017). "GDAS half-degree archive." 2016, from
1187 <ftp://arlftp.arlhq.noaa.gov/pub/archives/gdas0p5>, accessed 2016 and 2017.



- 1188 Noll, K. E. (1970): A rotary inertial impactor for sampling giant particles in the atmosphere. *Atmos.*
1189 *Environ.* 4, 9-19. doi: 10.1016/0004-6981(70)90050-8
- 1190 Noll, K. E., K. Y. P. Fang (1989): Development of a dry deposition model for atmospheric coarse
1191 particles. *Atmos. Environ.* 23(3), 585-594. doi: 10.1016/0004-6981(89)90007-3
- 1192 Noll, K. E., M. M. Jackson, A. K. Oskouie (2001): Development of an Atmospheric Particle Dry
1193 Deposition Model. *Aerosol Sci. Technol.* 35(2), 627-636. doi: 10.1080/02786820119835
- 1194 Noll, K. E., A. Pontius, R. Frey, M. Gould (1985): Comparison of atmospheric coarse particles at an
1195 urban and non-urban site. *Atmos. Environ.* 19(11), 1931-1943.
- 1196 Nowottnick, E., P. Colarco, A. da Silva, D. Hlavka, M. McGill (2011): The fate of saharan dust across
1197 the atlantic and implications for a central american dust barrier. *Atmos. Chem. Phys.* 11(16),
1198 8415-8431. doi: 10.5194/acp-11-8415-2011
- 1199 Ott, D. K., W. Cyrs, T. M. Peters (2008a): Passive measurement of coarse particulate matter, PM_{10-2.5}.
1200 *J. Aerosol Sci.* 39(2), 156-167. doi: 10.1016/j.jaerosci.2007.11.002
- 1201 Ott, D. K., T. Peters (2008b): A Shelter to Protect a Passive Sampler for Coarse Particulate Matter,
1202 PM_{10-2.5}. *Aerosol Sci. Technol.* 42, 299-309. doi: 10.1080/02786820802054236
- 1203 Paik, S., J. H. Vincent (2002): Aspiration efficiency for thin-walled nozzles facing the wind and for very
1204 high velocity ratios. *J. Aerosol Sci.* 33(5), 705-720. doi: 10.1016/S0021-8502(01)00208-7
- 1205 Pattengale, N. D., M. Alipour, O. R. P. Bininda-Emonds, B. M. E. Moret, A. Stamatakis (2010): How
1206 Many Bootstrap Replicates Are Necessary? *J. Comput. Biol.* 17(3), 337-354. doi:
1207 10.1089/cmb.2009.0179
- 1208 Petroff, A., L. Zhang (2010): Development and validation of a size-resolved particle dry deposition
1209 scheme for application in aerosol transport models. *Geosci. Model Dev.* 3(2), 753-769. doi:
1210 10.5194/gmd-3-753-2010
- 1211 Petters, M. D., S. M. Kreidenweis (2007): A single parameter representation of hygroscopic growth
1212 and cloud condensation nucleus activity. *Atmos. Chem. Phys.* 7(8), 1961-1971. doi:
1213 10.5194/acp-7-1961-2007
- 1214 Pinsky, M., A. Khain, M. Shapiro (1999): Collisions of Small Drops in a Turbulent Flow. Part I: Collision
1215 Efficiency. *Problem Formulation and Preliminary Results. J. Atmos. Sci.* 56(15), 2585-2600.
1216 doi: 10.1175/1520-0469(1999)056<2585:cosdia>2.0.co;2
- 1217 Piskunov, V. N. (2009): Parameterization of aerosol dry deposition velocities onto smooth and rough
1218 surfaces. *J. Aerosol Sci.* 40(8), 664-679. doi: 10.1016/j.jaerosci.2009.04.006
- 1219 Prospero, J. M., R. Arimoto (2009). *Atmospheric Transport and Deposition of Particulate Material to*
1220 *the Oceans A2 - Steele, John H. Encyclopedia of Ocean Sciences (Second Edition). Oxford,*
1221 *Academic Press: 248-257.*
- 1222 Prospero, J. M., F.-X. Collard, J. Molinié, A. Jeannot (2014): Characterizing the annual cycle of African
1223 dust transport to the Caribbean Basin and South America and its impact on the environment
1224 and air quality. *Global Biogeochem. Cy.* 28(7), 2013GB004802. doi: 10.1002/2013gb004802
- 1225 Rasband, W. S. (2015). "ImageJ." 1.47c. 2015.
- 1226 Reid, E. A., J. S. Reid, M. M. Meier, M. R. Dunlap, S. S. Cliff, A. Broumas, K. Perry, H. Maring (2003):
1227 Characterization of African dust transported to Puerto Rico by individual particle and size
1228 segregated bulk analysis. *J. Geophys. Res.* 108(D19), 8591. doi: 10.1029/2002JD002935
- 1229 Ro, C.-U., J. Osán, I. Szalóki, J. de Hoog, A. Worobiec, R. Van Grieken (2003): A Monte Carlo Program
1230 for Quantitative Electron-Induced X-ray Analysis of Individual Particles. *Anal. Chem.* 75, 851-
1231 859.
- 1232 Salter, M. E., E. Hamacher-Barth, C. Leck, J. Werner, C. M. Johnson, I. Riipinen, E. D. Nilsson, P. Zieger
1233 (2016): Calcium enrichment in sea spray aerosol particles. *Geophysical Research Letters*
1234 43(15), 8277-8285. doi: 10.1002/2016gl070275
- 1235 Savoie, D. L., J. M. Prospero, S. J. Oltmans, W. C. Graustein, K. K. Turekian, J. T. Merrill, H. Levy (1992):
1236 Sources of nitrate and ozone in the marine boundary layer of the tropical north Atlantic. *J.*
1237 *Geophys. Res.* 97(D11), 11575-11589. doi: 10.1029/92jd00894



- 1238 Scheuvens, D., K. Kandler, M. Küpper, K. Lieke, S. Zorn, M. Ebert, L. Schütz, S. Weinbruch (2011):
1239 Individual-particle analysis of airborne dust samples collected over Morocco in 2006 during
1240 SAMUM 1. Tellus 63B, 512-530. doi: 10.1111/j.1600-0889.2011.00554.x
- 1241 Schladitz, A., T. Müller, A. Nowak, K. Kandler, K. Lieke, A. Massling, A. Wiedensohler (2011): In situ
1242 aerosol characterization at Cape Verde Part 1: Particle number size distributions, hygroscopic
1243 growth and state of mixing of the marine and Saharan dust aerosol. Tellus 63B, 531-548. doi:
1244 10.1111/j.1600-0889.2011.00569.x
- 1245 Schütz, L. (1980): Long range transport of desert dust with special emphasis on the Sahara. Ann. NY
1246 Acad. Sci. 338(1), 515-532. doi: 10.1111/j.1749-6632.1980.tb17144.x
- 1247 Sedwick, P. N., E. R. Sholkovitz, T. M. Church (2007): Impact of anthropogenic combustion emissions
1248 on the fractional solubility of aerosol iron: Evidence from the Sargasso Sea. Geochem.
1249 Geophys. Geosy. 8(10). doi: doi:10.1029/2007GC001586
- 1250 Sehmel, G. A. (1973). Particle Deposition and Diffusivities Along Smooth Surfaces. Pollution. E. S.
1251 Barrekette, Springer. 2: 564-571.
- 1252 Shi, Z., M. D. Krom, S. Bonneville, A. R. Baker, C. Bristow, N. Drake, G. Mann, K. Carslaw, J. B.
1253 McQuaid, T. Jickells, L. G. Benning (2011a): Influence of chemical weathering and aging of
1254 iron oxides on the potential iron solubility of Saharan dust during simulated atmospheric
1255 processing. Global Biogeochem. Cy. 25, GB2010. doi: 10.1029/2010GB003837
- 1256 Shi, Z., M. D. Krom, T. D. Jickells, S. Bonneville, K. S. Carslaw, N. Mihalopoulos, A. R. Baker, L. G.
1257 Benning (2012): Impacts on iron solubility in the mineral dust by processes in the source
1258 region and the atmosphere: A review. Aeolian Res. 5, 21-42. doi:
1259 10.1016/j.aeolia.2012.03.001
- 1260 Shi, Z. B., M. T. Woodhouse, K. S. Carslaw, M. D. Krom, G. W. Mann, A. R. Baker, I. Savov, G. R. Fones,
1261 B. Brooks, N. Drake, T. D. Jickells, L. G. Benning (2011b): Minor effect of physical size sorting
1262 on iron solubility of transported mineral dust. Atmos. Chem. Phys. 11(16), 8459-8469. doi:
1263 10.5194/acp-11-8459-2011
- 1264 Sholkovitz, E. R., P. N. Sedwick, T. M. Church, A. R. Baker, C. F. Powell (2012): Fractional solubility of
1265 aerosol iron: Synthesis of a global-scale data set. Geochim. Cosmochim. Acta 89, 173-189.
1266 doi: 10.1016/j.gca.2012.04.022
- 1267 Slinn, S. A., W. G. N. Slinn (1980): Predictions for particles deposition on natural waters. Atmos.
1268 Environ. 14, 1013-1016. doi: 10.1016/0004-6981(80)90032-3
- 1269 Stein, A. F., R. R. Draxler, G. D. Rolph, B. J. B. Stunder, M. D. Cohen, F. Ngan (2015): NOAA's HYSPLIT
1270 Atmospheric Transport and Dispersion Modeling System. Bull. Am. Met. Soc. 96(12), 2059-
1271 2077. doi: 10.1175/bams-d-14-00110.1
- 1272 Stevens, B., D. Farrell, L. Hirsch, F. Jansen, L. Nuijens, I. Serikov, B. Brüggemann, M. Forde, H. Linne, K.
1273 Lonitz, J. M. Prospero (2016): The Barbados Cloud Observatory: Anchoring Investigations of
1274 Clouds and Circulation on the Edge of the ITCZ. Bull. Am. Met. Soc. 97(5), 787-801. doi:
1275 10.1175/bams-d-14-00247.1
- 1276 Sullivan, R. C., S. A. Guazzotti, D. A. Sodeman, K. A. Prather (2007a): Direct observations of the
1277 atmospheric processing of Asian mineral dust. Atmos. Chem. Phys. 7, 1213-1236. doi:
1278 10.5194/acp-7-1213-2007
- 1279 Sullivan, R. C., S. A. Guazzotti, D. A. Sodeman, Y. Tang, G. R. Carmichael, K. A. Prather (2007b):
1280 Mineral dust is a sink for chlorine in the marine boundary layer. Atmos. Environ. 41, 7166-
1281 7179. doi: 10.1016/j.atmosenv.2007.05.047
- 1282 Sundaram, S., L. R. Collins (1997): Collision statistics in an isotropic particle-laden turbulent
1283 suspension. Part 1. Direct numerical simulations. J. Fluid Mech. 335, 75-109. doi:
1284 10.1017/s0022112096004454
- 1285 Tang, M., D. J. Cziczo, V. H. Grassian (2016): Interactions of Water with Mineral Dust Aerosol: Water
1286 Adsorption, Hygroscopicity, Cloud Condensation, and Ice Nucleation. Chem. Rev. 116(7),
1287 4205-4259. doi: 10.1021/acs.chemrev.5b00529



- 1288 Trapp, J. M., F. J. Millero, J. M. Prospero (2010): Temporal variability of the elemental composition of
1289 African dust measured in trade wind aerosols at Barbados and Miami. *Mar. Chem.* 120, 71-
1290 82. doi: 10.1016/j.marchem.2008.10.004
- 1291 Trincavelli, J., S. Limandri, R. Bonetto (2014): Standardless quantification methods in electron probe
1292 microanalysis. *Spectrochim. Acta B* 101, 76-85. doi: 10.1016/j.sab.2014.07.016
- 1293 Ullerstam, M., R. Vogt, S. Langer, E. Ljungström (2002): The kinetics and mechanism of SO₂ oxidation
1294 by O₃ on mineral dust. *Phys. Chem. Chem. Phys.* 4, 4694-4699. doi: 10.1039/B203529B
- 1295 Usher, C. R., H. Al-Hosney, S. Carlos-Cuellar, V. H. Grassian (2002): A laboratory study of the
1296 heterogeneous uptake and oxidation of sulfur dioxide on mineral dust particles. *J. Geophys.*
1297 *Res.* 107(D23), 4713. doi: 10.1029/2002JD002051
- 1298 van der Does, M., L. F. Korte, C. I. Munday, G. J. A. Brummer, J. B. W. Stuut (2016): Particle size traces
1299 modern Saharan dust transport and deposition across the equatorial North Atlantic. *Atmos.*
1300 *Chem. Phys.* 16(21), 13697-13710. doi: 10.5194/acp-16-13697-2016
- 1301 Wagner, J., D. Leith (2001): Passive Aerosol Sampler. Part I: Principle of Operation. *Aerosol Sci.*
1302 *Technol.* 34(186-192). doi: 10.1080/027868201300034808
- 1303 Wang, L.-P., O. Ayala, S. E. Kasprzak, W. W. Grabowski (2005): Theoretical Formulation of Collision
1304 Rate and Collision Efficiency of Hydrodynamically Interacting Cloud Droplets in Turbulent
1305 Atmosphere. *J. Atmos. Sci.* 62(7), 2433-2450. doi: 10.1175/jas3492.1
- 1306 Warneck, P., J. Williams (2012): *The Atmospheric Chemist's Companion. Numerical Data for Use in*
1307 *the Atmospheric Sciences*, Springer Netherlands.
- 1308 Weinbruch, S., M. Wentzel, M. Kluckner, P. Hoffmann, H. M. Ortner (1997): Characterization of
1309 Individual Atmospheric Particles by Element Mapping in Electron Probe Microanalysis.
1310 *Mikrochim. Acta* 125, 137-141. doi: 10.1007/BF01246176
- 1311 Weinzierl, B., A. Ansmann, J. M. Prospero, D. Althausen, N. Benker, F. Chouza, M. Dollner, D. Farrell,
1312 W. K. Fomba, V. Freudenthaler, J. Gasteiger, S. Groß, M. Haarig, B. Heinold, K. Kandler, T. B.
1313 Kristensen, O. L. Mayol-Bracero, T. Müller, O. Reitebuch, D. Sauer, A. Schäfler, K. Schepanski,
1314 A. Spanu, I. Tegen, C. Toledano, A. Walser (2017): The Saharan Aerosol Long-Range Transport
1315 and Aerosol-Cloud-Interaction Experiment: Overview and Selected Highlights. *Bulletin of the*
1316 *American Meteorological Society* 98(7), 1427-1451. doi: 10.1175/bams-d-15-00142.1
- 1317 Weinzierl, B., D. Sauer, M. Esselborn, A. Petzold, A. Veira, M. Rose, S. Mund, M. Wirth, A. Ansmann,
1318 M. Tesche, S. Gross, V. Freudenthaler (2011): Microphysical and optical properties of dust
1319 and tropical biomass burning aerosol layers in the Cape Verde region—an overview of the
1320 airborne in situ and lidar measurements during SAMUM-2. *Tellus B* 63(4), 589-618. doi:
1321 10.1111/j.1600-0889.2011.00566.x
- 1322 Wen, X., D. B. Ingham (2000): Aspiration efficiency of a thin-walled cylindrical aerosol sampler at yaw
1323 orientations with respect to the wind. *J. Aerosol Sci.* 31(11), 1355-1365. doi: 10.1016/S0021-
1324 8502(00)00036-7
- 1325 Wood, N. B. (1981): A simple method for the calculation of turbulent deposition to smooth and rough
1326 surfaces. *J. Aerosol Sci.* 12(3), 275-290. doi: 10.1016/0021-8502(81)90127-0
- 1327 Worringen, A., K. Kandler, N. Benker, T. Dirsch, S. Mertes, L. Schenk, U. Kästner, F. Frank, B. Nillius, U.
1328 Bundke, D. Rose, J. Curtius, P. Kupiszewski, E. Weingartner, P. Vochezer, J. Schneider, S.
1329 Schmidt, S. Weinbruch, M. Ebert (2015): Single-particle characterization of ice-nucleating
1330 particles and ice particle residuals sampled by three different techniques. *Atmos. Chem.*
1331 *Phys.* 15(8), 4161-4178. doi: 10.5194/acp-15-4161-2015
- 1332 Xu, X., U. S. Akhtar (2010): Identification of potential regional sources of atmospheric total gaseous
1333 mercury in Windsor, Ontario, Canada using hybrid receptor modeling. *Atmos. Chem. Phys.*
1334 10(15), 7073-7083. doi: 10.5194/acp-10-7073-2010
- 1335 Zamora, L. M., J. M. Prospero, D. A. Hansell (2011): Organic nitrogen in aerosols and precipitation at
1336 Barbados and Miami: Implications regarding sources, transport and deposition to the
1337 western subtropical North Atlantic. *J. Geophys. Res.* 116(D20). doi:
1338 doi:10.1029/2011JD015660



- 1339 Zhang, D. (2008): Effect of sea salt on dust settling to the ocean. *Tellus* 60B, 641-646. doi:
1340 10.1111/j.1600-0889.2008.00358.x
- 1341 Zhang, D., Y. Iwasaka (1999): Nitrate and sulfate in individual Asian dust-storm particles in Beijing,
1342 China in spring of 1995 and 1996. *Atmos. Environ.* 33, 3213-3223. doi: 10.1016/S1352-
1343 2310(99)00116-8
- 1344 Zhang, D., Y. Iwasaka (2004): Size change of Asian dust particles caused by sea salt interaction:
1345 Measurements in southwestern Japan. *Geophys. Res. Lett.* 31, L15102. doi:
1346 10.1029/2004GL020087
- 1347
- 1348
- 1349
- 1350



1351

1352 **Table 1: Relationships between area coverage of the simulated 5 mm x 5 mm analysis field, particle numbers, particle**
 1353 **masses and uncertainties. Upper part: CV-ground size distribution, lower part: CV-air size distribution. A bulk density of**
 1354 **2500 kg/m³ was assumed for the mass estimation from particle volume. Abbreviations: SP coverage = ratio of the sum of**
 1355 **single particle cross sections to the analysis field; apparent coverage = fraction of area covered by the particles after**
 1356 **deposition; N_{>1} = Number of particles larger than 1 µm diameter; PM_{>1} = Total mass of particles larger than 1 µm**
 1357 **diameter (approx. 99.99 % of total mass); PM₁₋₃₂ = total mass of particles between 1 µm and 32 µm diameter (approx. 50**
 1358 **% of total mass for source-near size distribution, 67 % for aged one). Relative uncertainty is given as the ratio of the**
 1359 **upper and lower bounds of the central 95 % quantile to the median of 1000 (200 for SP coverage >= 0.1) repetitions of**
 1360 **deposition simulation.**

SP coverage	Apparent coverage	N _{>1}	PM _{>1} , µg	relative uncertainty	PM ₁₋₃₂ , µg	relative uncertainty
0.001	0.001	353	0.8	0.38 - 4.16	0.5	0.56 - 1.38
0.003	0.002	865	2.7	0.37 - 4.68	1.3	0.69 - 1.24
0.005	0.005	1699	4.6	0.53 - 3.60	2.5	0.78 - 1.18
0.006	0.006	2032	6.1	0.49 - 2.80	3.0	0.81 - 1.17
0.007	0.007	2361	6.9	0.54 - 2.76	3.5	0.82 - 1.16
0.008	0.008	2692	7.6	0.56 - 2.59	4.0	0.83 - 1.14
0.009	0.009	3016	8.3	0.58 - 2.57	4.5	0.84 - 1.14
0.010	0.010	3344	10	0.54 - 2.21	5.0	0.85 - 1.13
0.011	0.011	3669	11	0.57 - 2.26	5.5	0.85 - 1.13
0.012	0.012	3988	11	0.63 - 2.18	5.9	0.86 - 1.12
0.013	0.013	4313	13	0.64 - 2.03	6.4	0.87 - 1.12
0.015	0.015	4951	14	0.67 - 1.95	7.4	0.88 - 1.11
0.020	0.020	6520	20	0.69 - 2.09	9.8	0.89 - 1.10
0.025	0.025	8047	24	0.74 - 1.94	12	0.90 - 1.09
0.035	0.034	10998	34	0.77 - 1.71	17	0.92 - 1.07
0.050	0.048	15146	56	0.69 - 1.48	24	0.93 - 1.06
0.075	0.071	21379	81	0.75 - 1.45	36	0.94 - 1.05
0.100	0.093	26824	106	0.79 - 1.35	47	0.95 - 1.05
0.200	0.172	34099	218	0.80 - 1.53	89	0.97 - 1.04
0.001	0.001	1031	0.7	0.44 - 3.05	0.5	0.66 - 1.33
0.005	0.005	5056	3.6	0.73 - 1.84	2.4	0.84 - 1.15
0.010	0.010	9990	8.1	0.71 - 1.42	4.8	0.89 - 1.11
0.025	0.025	24102	19.8	0.79 - 1.27	11.9	0.93 - 1.07
0.050	0.048	45618	39.4	0.82 - 1.38	23.4	0.95 - 1.05
0.075	0.071	64665	59.1	0.85 - 1.29	34.6	0.96 - 1.04
0.100	0.093	81568	78.5	0.89 - 1.23	45.4	0.97 - 1.04
0.150	0.134	109224	118	0.90 - 1.17	65.7	0.97 - 1.03
0.200	0.173	129769	158	0.91 - 1.13	84.2	0.97 - 1.02

1361

1362



1363

1364 **Table 2: Average dust mass concentrations estimated from deposited particle mass applying various deposition models.**
 1365 Lower and upper refer to different dust fraction estimates (see Eq. (6) and (12)).

Model	lower estimate, $\mu\text{g}/\text{m}^3$	upper estimate, $\mu\text{g}/\text{m}^3$
Stokes settling	149	195
Noll et al. (2001)	0.28	0.32
Noll et al. (1989)	67	96
Aluko et al. (2006)	58	85
Piskunov (2009)	32	47
Wagner et al. (2001)	81	115
High-volume sampler		26

1366

1367

1368



1369

1370 Fig. 1: Comparison of the Na/Cl ratio of sodium chloride powder as function of particle size, corrected by the methods
1371 Cliff-Lorrimer, ZAF and interpolated. Measurements were performed at 20 kV acceleration voltage. The sodium chloride
1372 nominal ratio is shown as orange line. The linear regression of the interpolated correction is shown as black striped line.

1373

1374 Fig. 2: Calculated ion balance for all beam interaction volumes containing particles dominated by Na and Cl. Particles
1375 were collected by the DPDS. The axes are scaled in arbitrary units of percent \times unit charges. Smaller particles yield
1376 smaller values as they only fill a fraction of the beam interaction volume. Particle size is color-coded; note that all
1377 particles between 0.6 μm and 1 μm in size are shown as blue, and between 10 μm and 25 μm as red. The black diagonal
1378 lines show the 10 % deviation cone.

1379

1380 Fig. 3: Mean element index only using Na, Mg, S, Cl, and Ca for normalization, and according standard deviation (1 σ) for
1381 NaCl-dominated particles from a typical atmospheric sample as function of particle size. Note that relative standard
1382 deviation for Ca is not shown due to frequent values below the detection limit.

1383

1384 Fig. 4: Comparison of the relative two-sided 95 % confidence interval limits for bootstrap and Poisson approaches. Values
1385 shown are the confidence interval limits for the total deposited particle volume divided by this volume. Data basis are
1386 the deposition samples at Ragged Point of 2013. Left: for all particles; right: for particles between 1 μm and 20 μm
1387 diameter. The color shows the fraction of the total volume present in the single largest particle. Note the different scales
1388 between the graphs.

1389

1390 Fig. 5: Deposition velocity to a smooth surface calculated by different deposition models for the samples of 2013, taking
1391 into account the ambient thermodynamic conditions and the particle composition. a: Stokes settling; b: Noll et al. (2001);
1392 c: Noll et al. (1989); d: Aluko et al. (2006); e: Piskunov (2009) ; f: Wagner et al. (2001)

1393

1394 Fig. 6: Number (left column) and volume size distributions (right column) of deposition rates as function of projected
1395 area diameter modeled for Cape Verde aerosol as derived from a 5 mm \times 5 mm analysis field. The upper row is based on
1396 CV-ground, the lower on CV-air size distributions. The grey curve shows the original size distribution of deposited
1397 particles, the colored points with whiskers give median and central 95 % quantile of 1000 repetitions (200 for 0.093 and
1398 0.172/0.173) for distributions calculated from samples with different area fractions covered by particles.

1399

1400 Fig. 7: Number (left column) and volume size distributions (right column) of deposited particles measured at Ragged
1401 Point and extrapolated change as function of particle projected area diameter and area coverage fraction, simulating a
1402 longer exposure time. Different colors show different factors of exposure increase (5x, 10x, 15x, 20x). Resulting coverage
1403 fractions are given in the figure keys.

1404

1405 Fig. 8: Particle volume per area calculated from single particle measurements as function of the fractional area coverage.
1406 Blue symbols denote the unmodified samples, red symbols the simulation of higher coverage by factors of 2, 3, 5, 10, 15,
1407 and 20. Error bars denote the two-sided 95 % confidence interval. The fit function shown as black dashed line is
1408 calculated as $= \exp(a \ln(x) + b)$; $[y] = \text{mm}^3/\text{m}^2$; $a = 0.957 \pm 0.041$; $b = 3.57 \pm 0.06$; x is the fractional area
1409 coverage.

1410



1411

1412 **Fig. 9: Upper 95 % quantile of the fractions of internally mixed particles due to coincidental mixture on the substrate**
1413 **(color scale) as function of the projected area diameter and substrate area coverage, for a two-component system.**
1414 **Strong mixture refers to a minimum particle volume fraction of the other component of 20 %, detectable mixture refers**
1415 **to 1 %. Ratios of the two components in the base aerosol are given as percentages above each plot.**

1416

1417 **Fig. 10: Upper 95 % quantile of the fractions of internally mixed particles due to coincidental mixing on the substrate**
1418 **(color scale), for a dust/sea-salt/sulfate system with measured composition and CV-ground size distribution. Strong**
1419 **mixture refers to a minimum particle volume fraction of the other component of 20 %, detectable mixture refers to 1 %.**
1420 **Mixing compounds are given on top of each graph. Sulfate/sea-salt and ternary mixtures practically do not form**
1421 **coincidentally.**

1422

1423 **Fig. 11: Average atmospheric mass size distribution densities derived from DPDS and FWI measurements. Left: period**
1424 **from July 10 to 15, 2013; right: from June 14 to July 8, 2013. Different colors refer to different deposition velocity**
1425 **estimates as shown in Fig. 5. Solid lines refer to total mass concentrations, dashed ones to the dust mass estimated from**
1426 **the chemical composition (upper limit estimate). Error bars show the central 95 % confidence interval. Pink crosses show**
1427 **a size distribution measured in the Saharan air layer on June 22, 2013 (Weinzierl et al. 2017). Note that for particles**
1428 **smaller than 10 μm the FWI data may contain a considerable bias in calculation.**

1429

1430 **Fig. 12: Dust mass concentration and flux density time series derived from DPDS compared to such obtained from high-**
1431 **volume sampler (Kristensen et al. 2016). The darker brown bar shows the range from lower to upper estimate, the blue**
1432 **triangles the lower and upper estimate of dust deposition flux density. The date refers to the year 2013.**

1433

1434 **Fig. 13: Size dependence of the relative number abundance of major particle types as derived from single particle**
1435 **analysis of deposited aerosol.**

1436

1437 **Fig. 14: Left: box plot of daily mass deposition rate for total dust and dust-derived elements at Barbados for 2013 and**
1438 **2016. Right: cumulative mass deposition flux as function of aerodynamic particle diameter for dust and dust-derived**
1439 **elements. Note that for P and Ti in the latter plot two particles containing each more than 10 % of the total deposited**
1440 **mass have been removed from the data set.**

1441

1442 **Fig. 15: Potential source contribution functions (PSCF) of deposited material: dust (upper row), total soluble sulfate**
1443 **(central row) and relative ion balance for sulfate particles (lower row) for 2013 and 2016 at Ragged Point. Note that for**
1444 **dust, potential provenance is calculated for Saharan Air Layer transport only (i.e. trajectory arrival altitudes > 1500 m).**

1445

1446 **Fig. 16: Iron availability (SIAI) and deposition potential source contribution functions (PSCF) for 2013 and 2016. Upper**
1447 **row: geometric iron availability index, only silicate particles counted; trajectories arriving 1500–3000 m over Ragged**
1448 **Point. Lower row: mass deposition rate of Fe-rich particles smaller than 4 μm in diameter; trajectories arriving lower**
1449 **than 1500 m over Ragged Point.**

1450

1451 **Fig. 17: Ca/Na atomic ratio as function of particle dry diameter for all sea-salt particles collected at Ragged Point in 2013.**
1452 **Different samplers are shown by color: CI blue, DPDS red, and FWI brown**



1453

1454 **Fig. 18: Time-series of wind and particle number deposition rates for pure compounds and internally mixed particles for**
1455 **June/July 2013 and August 2016. Particle size ranges are given in the top left of each graph. The limit of detection for the**
1456 **number of internally mixed particles is shown as line in the according color. Where only the detection limit for**
1457 **silicate/sulfate mixtures is visible, both limits are identical.**

1458

1459 **Fig. 19: Deposition velocities calculated with the Piskunov model for internal admixture of sea-salt (left) or sulfate (right)**
1460 **for the mixed particles observed at Ragged Point. Velocities are given for the unmixed dust core and internal mixtures at**
1461 **dry conditions, at ambient relative humidity, and at 90 % relative humidity. The lines show the according means. Note**
1462 **that variation in deposition velocity for the same dust core size arises from variation in wind speed and admixed fraction.**

1463

1464 **Fig. 20: Effective deposition velocity for all dust-containing particles observed at Ragged Point. The blue curves take into**
1465 **account internal mixing and hygroscopic growth at ambient conditions, whereas the orange only regards the dry dust**
1466 **fraction of the particles. In addition, cumulative mass distribution is shown on the inverted right axis. Particle size is**
1467 **given as aerodynamic diameter for the dust fraction of a particle. For the ambient deposition velocity, the geometric**
1468 **mean for each size class is shown in conjunction with the 1 geometric standard deviation range.**

1469



Fig. 01

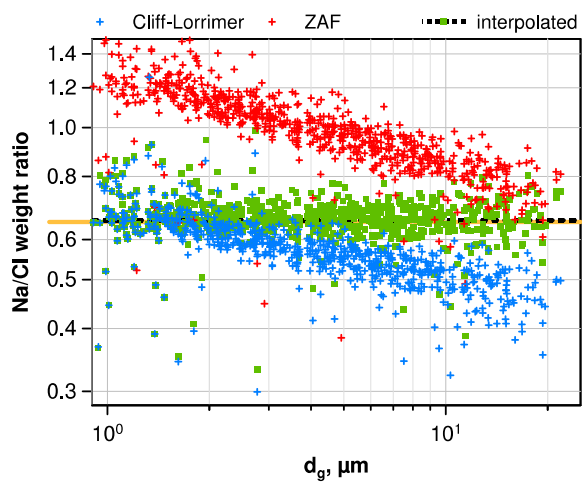




Fig. 02

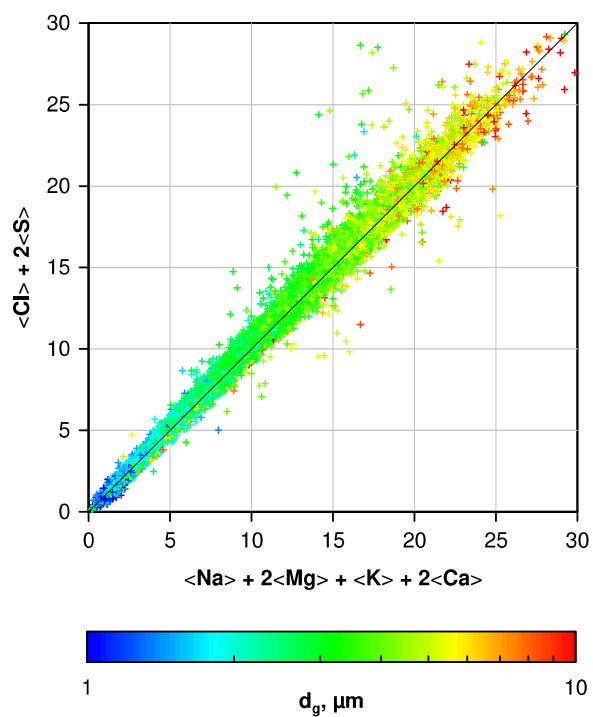




Fig. 03

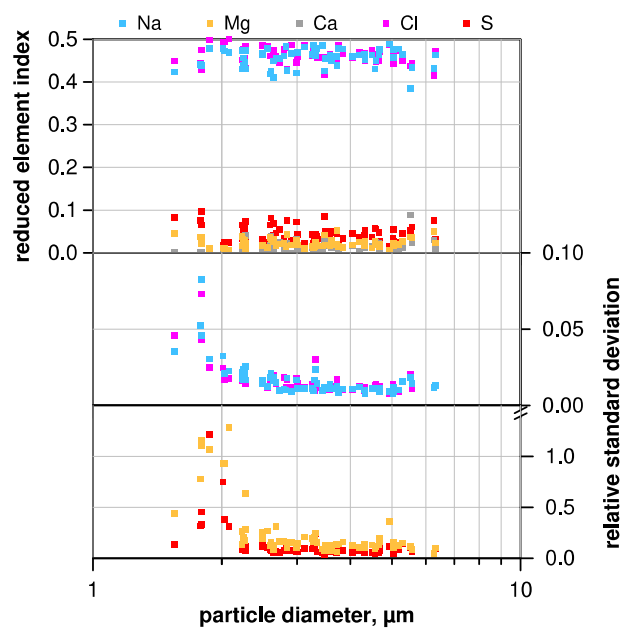




Fig. 04

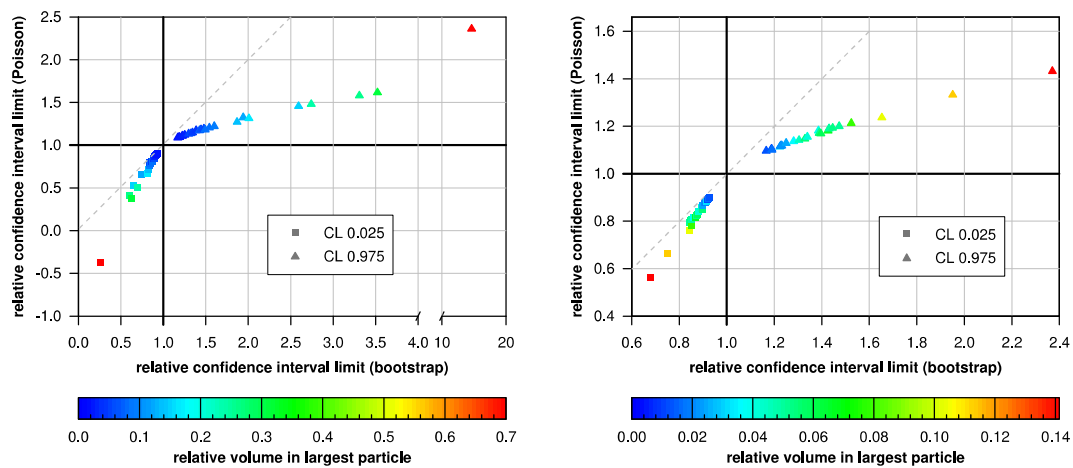




Fig. 05

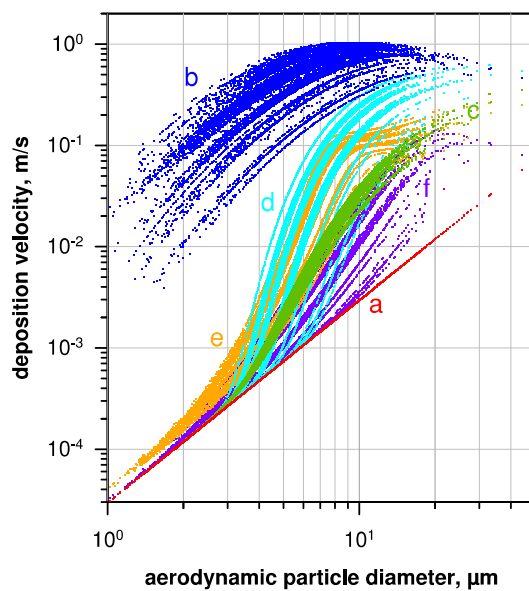




Fig. 06

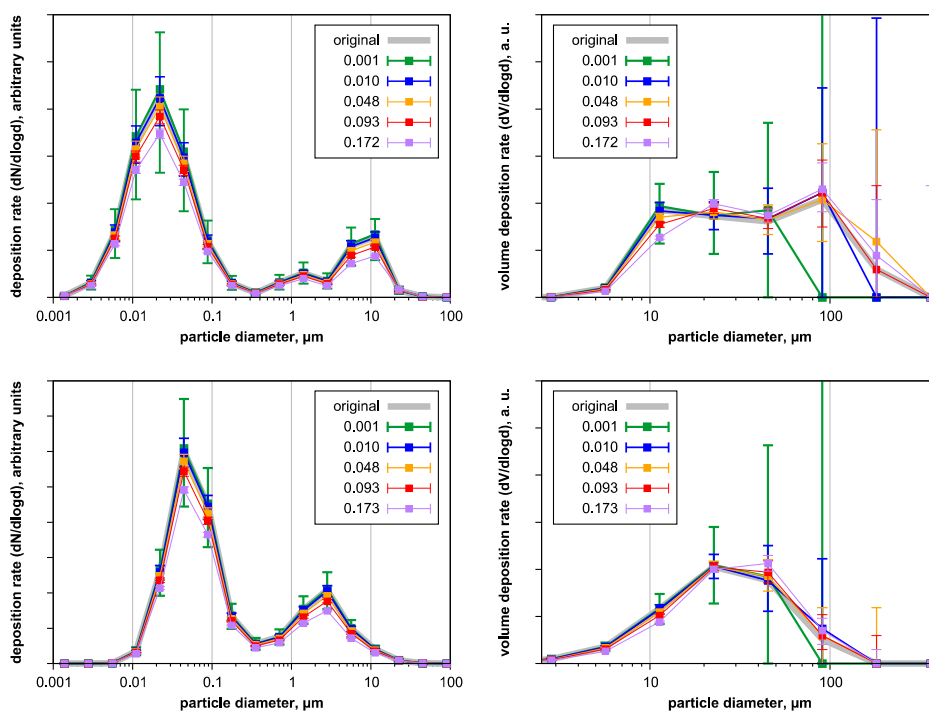




Fig. 07

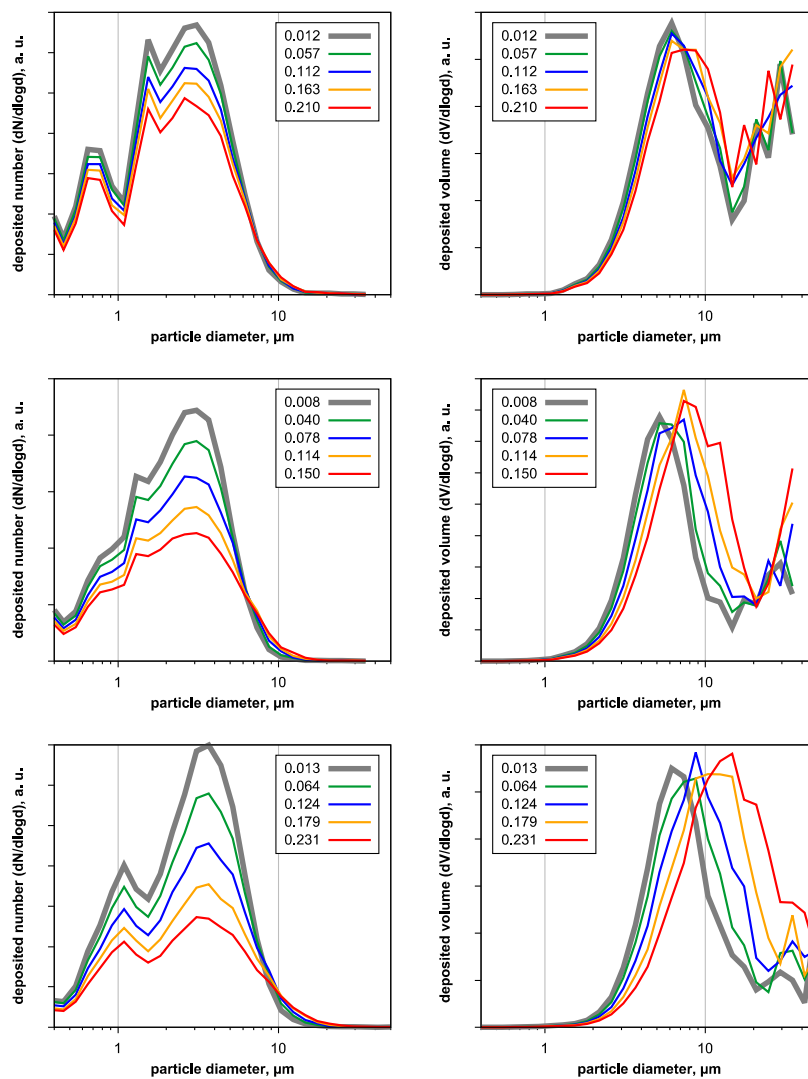




Fig. 08

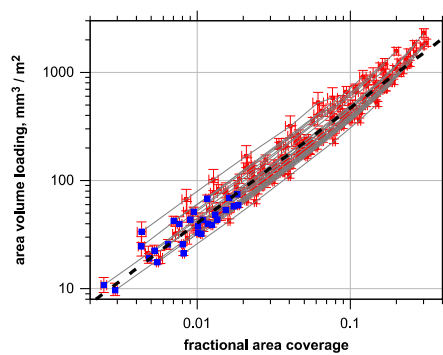




Fig. 09

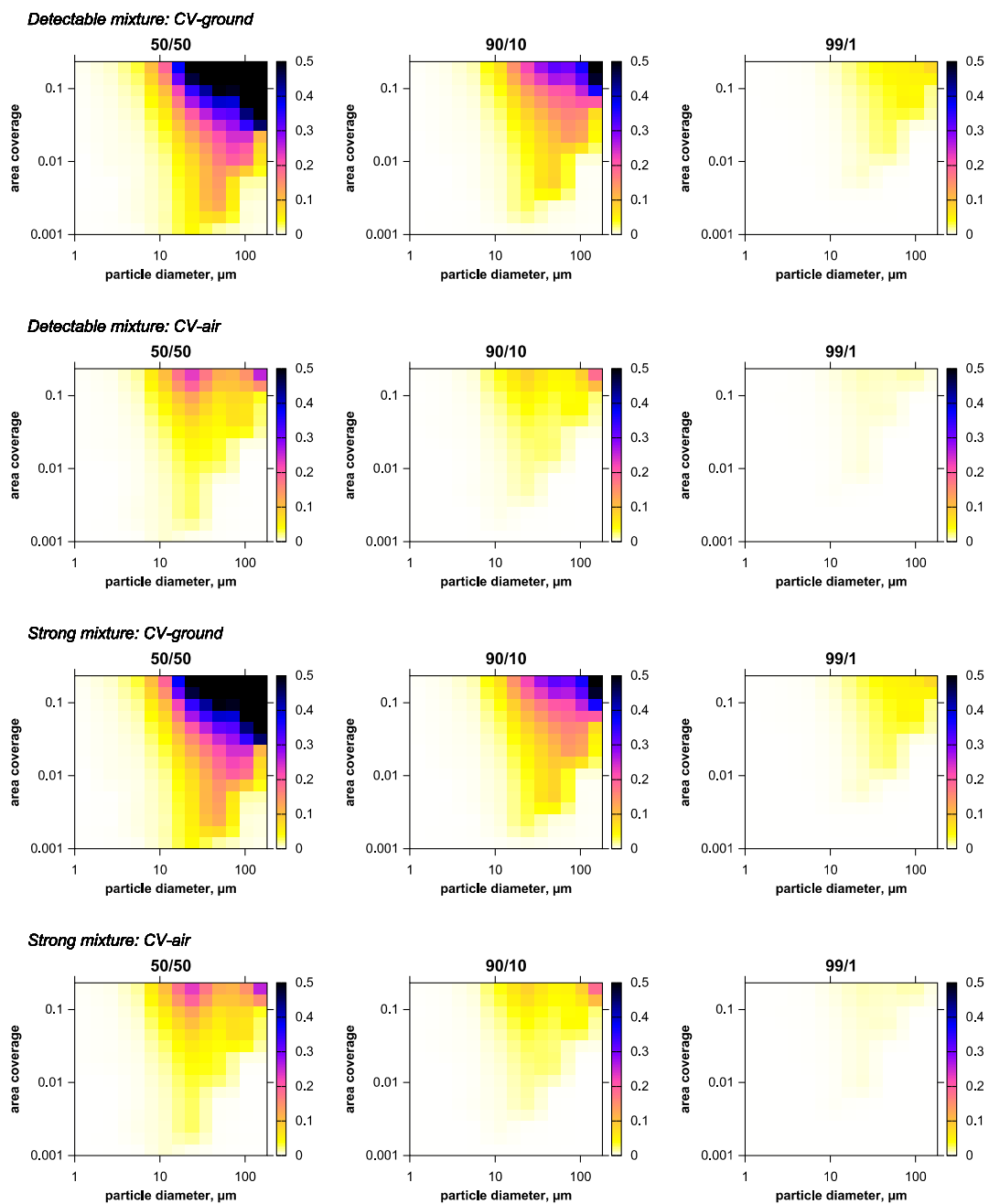




Fig. 10

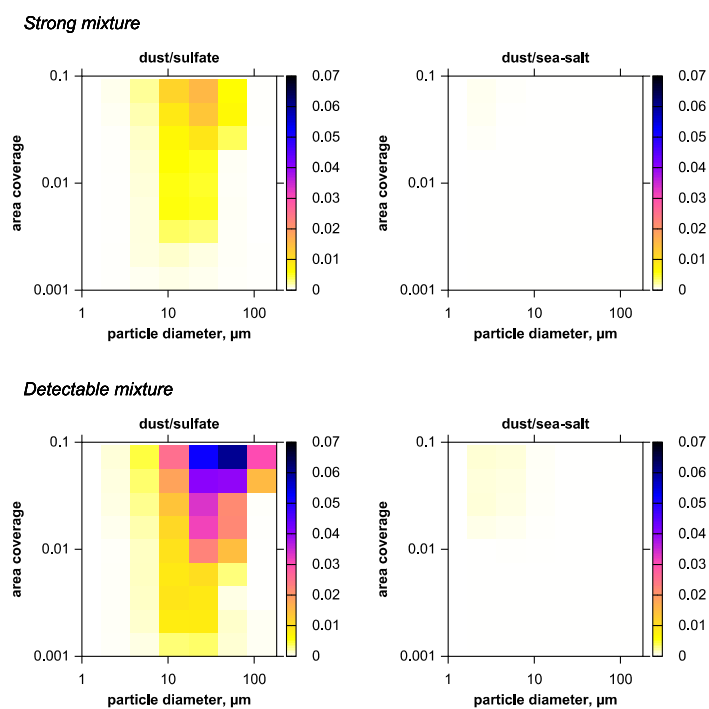




Fig. 11

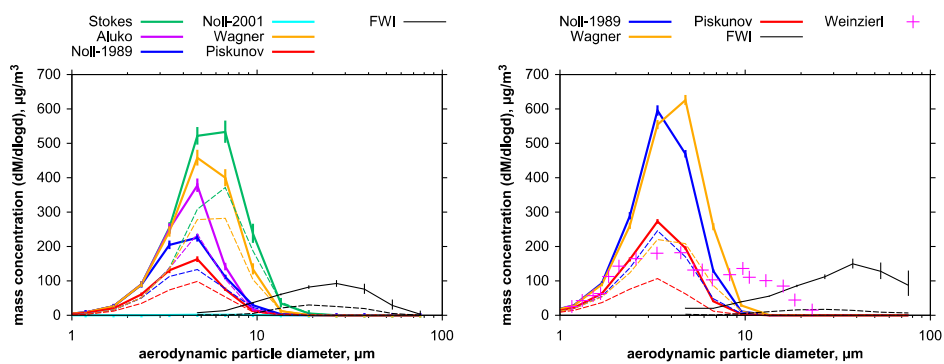




Fig. 12

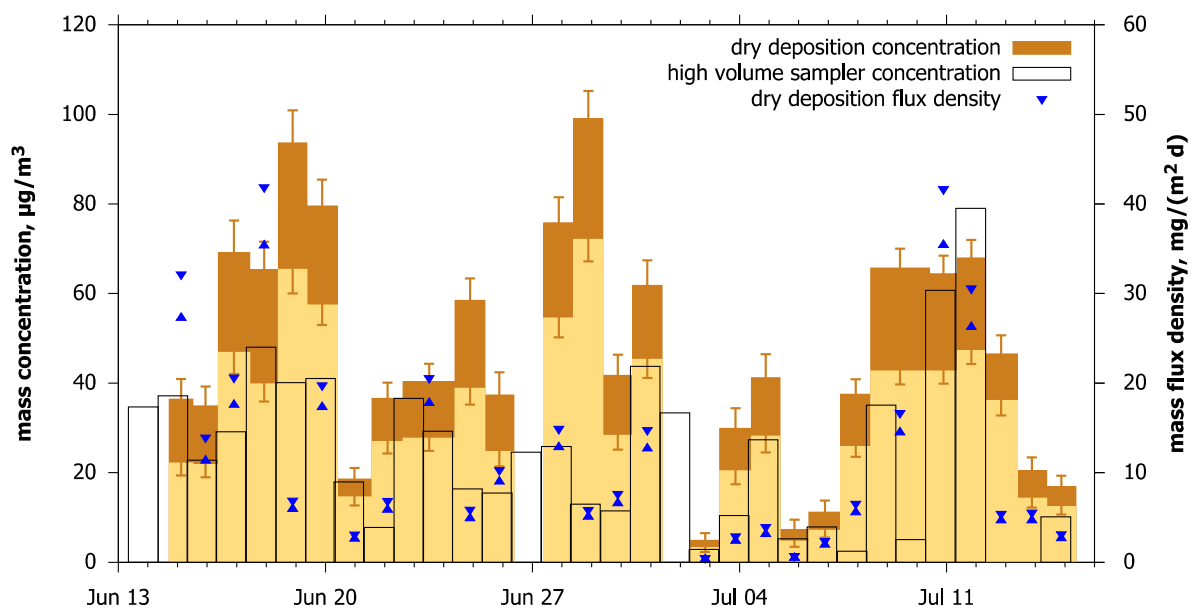




Fig. 13

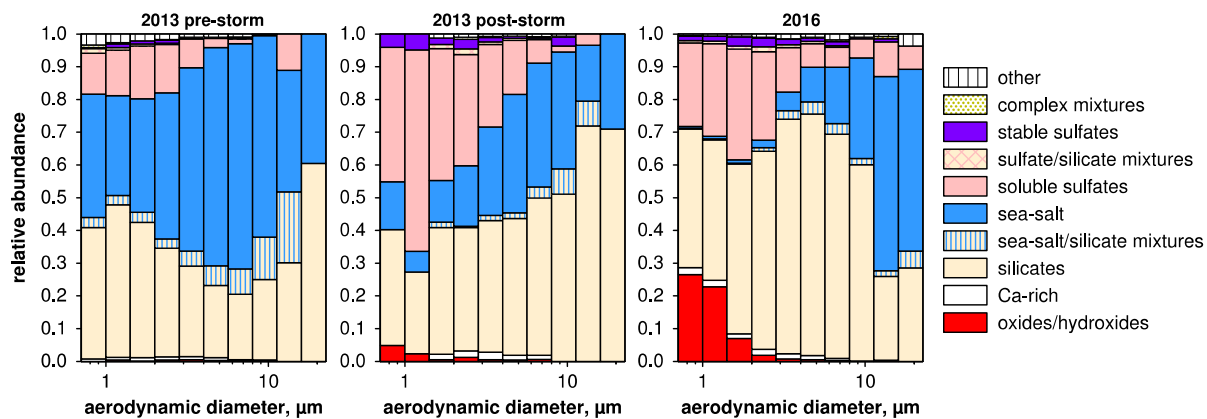




Fig. 14

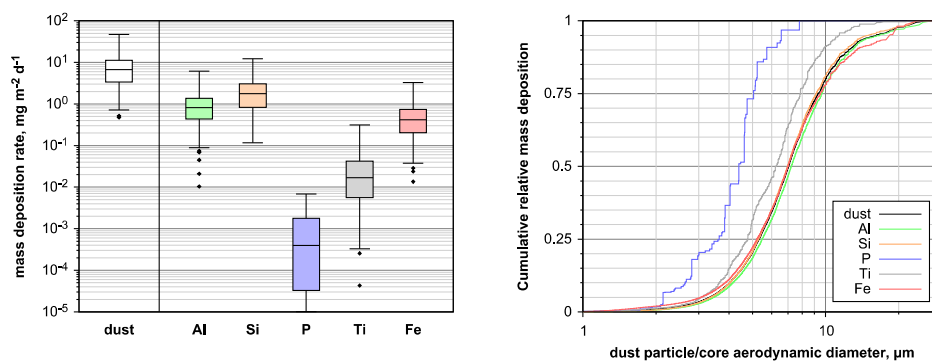




Fig. 15

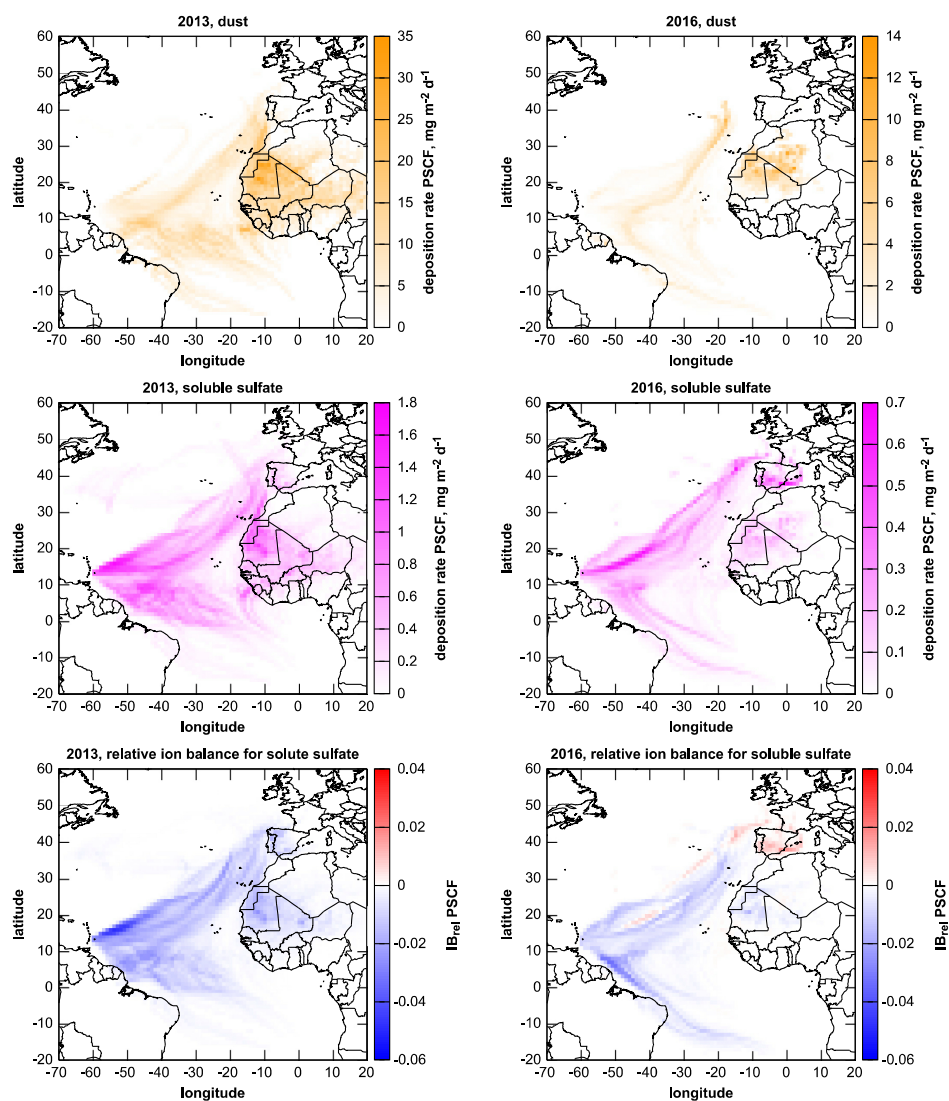




Fig. 16

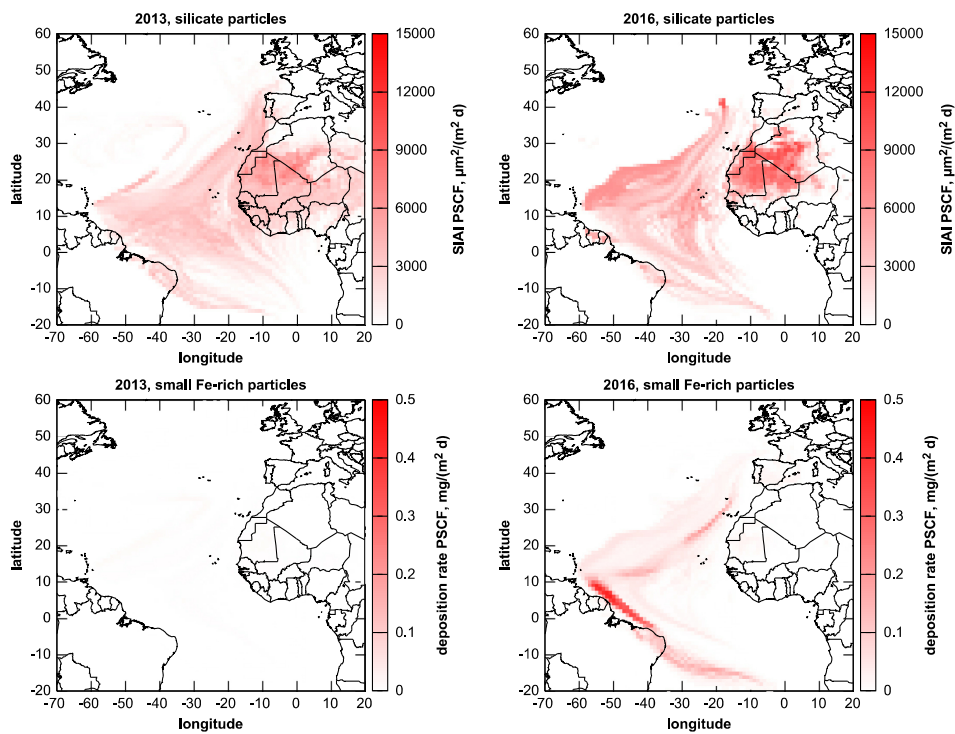




Fig. 17

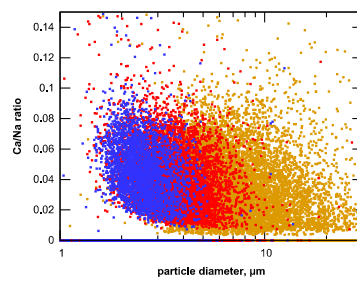




Fig. 18

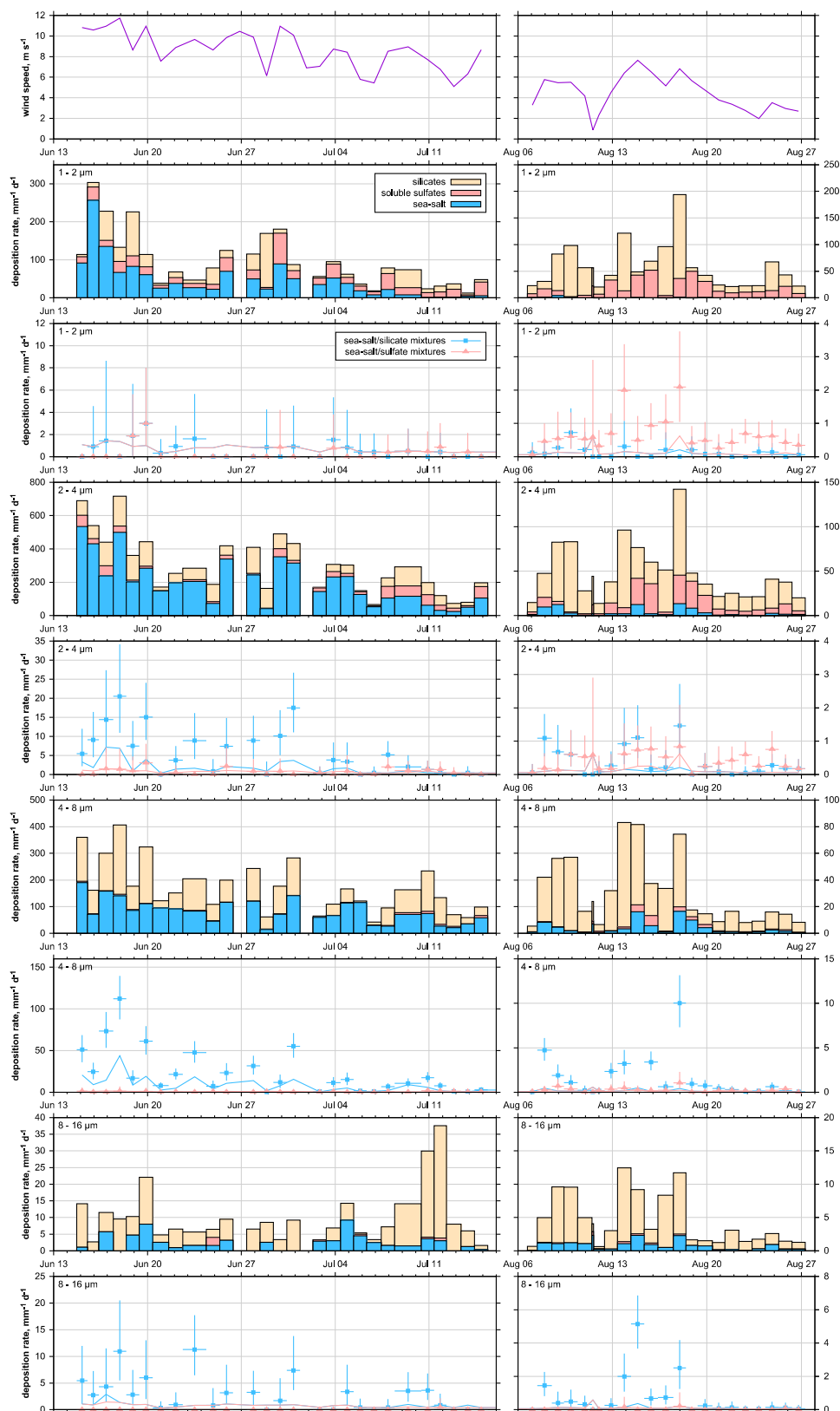




Fig. 19

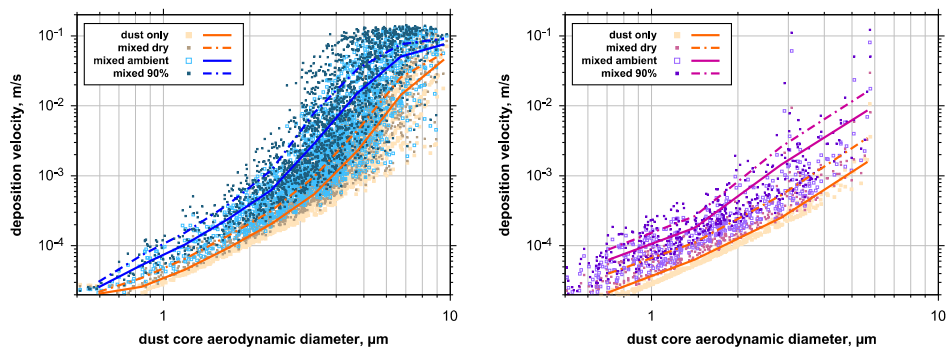




Fig. 20

